

**NASA CONTRACTOR
REPORT**

NASA CR-1990



NASA CR-1

0061278



**LOAN COPY: RETURN TO
AFWL (DOUL)
KIRTLAND AFB, N. M.**

**EVALUATION OF ONE-DIMENSIONAL
APPROXIMATIONS FOR RADIATIVE
TRANSPORT IN BLUNT BODY SHOCK LAYERS**

by K. H. Wilson

Prepared by

LOCKHEED MISSILES & SPACE COMPANY

Sunnyvale, Calif.

for Ames Research Center

NATIONAL AERONAUTICS AND SPACE ADMINISTRATION • WASHINGTON, D. C. • MARCH 1972



0061278

1. Report No. NASA CR-1990		2. Government Accession No.		3. Recipient's Catalog No.	
4. Title and Subtitle "Evaluation of One-Dimensional Approximations for Radiative Transport in Blunt Body Shock Layers"				5. Report Date March 1972	
				6. Performing Organization Code	
7. Author(s) K. H. Wilson				8. Performing Organization Report No.	
9. Performing Organization Name and Address Lockheed Missiles & Space Company Sunnyvale, California				10. Work Unit No.	
				11. Contract or Grant No. NAS 2-5749	
12. Sponsoring Agency Name and Address National Aeronautics & Space Administration Washington, D.C. 20546				13. Type of Report and Period Covered Contractor Report.	
				14. Sponsoring Agency Code	
15. Supplementary Notes					
16. Abstract One-dimensional approximations for the nongray radiative flux and flux divergence in radiating shock layers about a blunt entry body are compared with an exact three-dimensional treatment. A coupled radiative-gasdynamics analysis of the shock layer flow about the entire body provided the thermodynamic field used in these comparisons. In terms of calculating the total energy lost by the shock layer, the one-dimensional approximations to the radiative flux divergence are accurate to within a few percent. In terms of calculating the surface flux, the one-dimensional approximations introduce the largest errors of ~15% near the stagnation point. The source of these errors is the slab-like geometric representation of the shock layer inherent in all one-dimensional models. Finally, for both the radiative flux and its divergence, the tangent slab approximation provides more accurate results than differential approximation methods. <i>1. Radiation flux - Yoon</i> <i>2. Blunt body</i> <i>3. Shock waves</i> <i>4. approximations</i>					
17. Key Words (Suggested by Author(s)) Radiative transport Shock Layer One-Dimensional approximation			18. Distribution Statement UNCLASSIFIED-UNLIMITED		
19. Security Classif. (of this report) UNCLASSIFIED		20. Security Classif. (of this page) UNCLASSIFIED		21. No. of Pages 66	22. Price* 3.00

ABSTRACT

A study has been made of the accuracy of various one-dimensional approximations for calculating the radiative flux and flux divergence in the thin radiating shock layer surrounding a blunt entry body. The one-dimensional approximations were the tangent slab and the full and half range differential methods. A numerical calculation of the exact three-dimensional radiative transport equations provided a reference against which the one-dimensional models could be judged. A coupled radiative-gasdynamics analysis of the shock layer flow about the entire body provided the thermodynamic field used in these calculations. The radiative properties model employed was a three-group treatment of the continuum emission/absorption processes of high temperature air. In terms of calculating the total energy lost by the shock layer, the one-dimensional approximations to the radiative flux divergence are accurate to within a few percent. In terms of calculating the surface flux, the one-dimensional approximations introduce the largest errors near the stagnation point where the errors are about 15%. The source of these errors is the slab-like geometric representation of the shock layer inherent in all one-dimensional models. Finally, it is found that for both the radiative flux and its divergence, the tangent slab approach generally provides the most accurate results when compared with the differential approximation methods.

FOREWORD

This report is one of two volumes covering work performed for the National Aeronautics and Space Administration, Ames Research Center, Moffett Field, California under the terms and specifications of Contract NAS 2-5749. The period of technical performance of the contract was from 10 January 1970 to 7 April 1971. Technical monitor for this contract was Mr. William Page, Hypersonic Free-Flight Branch.

The work carried out under this contract was performed at the Lockheed Palo Alto Research Laboratory, Fluid Mechanics Laboratory, W. C. Marlow, Manager. Principal investigators for this contract were Ken Wilson and Dr. Y. S. Chou.

NOMENCLATURE

A	exponential integral emissivity function
a_0, a_1	parameters in number density equations
a	parameter in shock and body conic section equation, dimensionless
B	Planck function, $W/cm^2 sr$
b	parameter in shock and body conic section equation, dimensionless
c_0, c_1	constant in the boundary conditions for the differential approximations, W/cm^2
c	parameter in the boundary conditions for the differential approximations, W/cm^2
E	emissivity function, dimensionless
F	radiative flux, W/cm^2
H	total enthalpy, erg/gm
h	static enthalpy, erg/gm
I	radiative intensity, $W/cm^2 sr$
k	Boltzman constant, $8.617 \times 10^{-5} eV/^{\circ}K$
L	coordinate parallel to ϕ -constant plane, dimensionless
l	parameter defining full- or half-range differential approximation, dimensionless
N_t	total particle number density, cm^{-3}
N_a	air atom concentration, cm^{-3}
N	coordinate along rotation axis, dimensionless
p	pressure, atm
R	gas constant, erg/gm

R_n	nose radius, m
r	radial coordinate, dimensionless
s	distance along ray, dimensionless
T	temperature, °K
U_∞	freestream velocity, km/sec
U	angular averaged intensity, W/cm^2
x	body oriented streamwise coordinate, dimensionless
y	body oriented normal coordinate, dimensionless
z	axial coordinate, dimensionless

Greek Nomenclature

α_o	parameter in differential approximation flux equation, dimensionless
β_i	ionization parameter, dimensionless
β_d	dissociation parameter, dimensionless
ϵ	wall emissivity, dimensionless
ϵ	exponential integral, dimensionless
ρ_∞	freestream density, gm/cm^3
μ	volumetric absorption coefficient, cm^{-1}
Ψ	Planck function integral for differential approximation flux equations, W/cm^2
φ	azimuthal angular coordinate measured about rotation axis, radians
θ	elevation angular coordinate measured from rotation axis, radians
θ^*	critical value of elevation angle, radians
Ω	solid angle, steradians
δ_o	stagnation point shock layer thickness

Superscripts

- + denotes flux or intensity directed toward shock
- denotes flux or intensity directed toward body

Subscripts

- t denotes tangent point of conical shock or body
- o denotes point in shock layer at which flux is evaluated
- b denotes body condition
- s denotes shock condition
- m denotes maximum ray length
- x denotes flux component in x coordinate direction
- y denotes flux component in y coordinate direction
- z denotes flux component in z coordinate direction
- r denotes flux component in r coordinate direction

TABLE OF CONTENTS

<u>Section</u>	<u>Page</u>
ABSTRACT	i
FOREWORD	ii
NOMENCLATURE	iii
1. INTRODUCTION	1
2. THREE-DIMENSIONAL CALCULATIONS	4
2.1 Geometric Considerations	4
2.2 Angular Integrations	16
2.3 Gasdynamic, Thermodynamic and Radiation Transport Properties	21
3. ONE-DIMENSIONAL TRANSPORT	26
3.1 Solution for the Intensity	26
3.2 Slab Approximation for the Flux	27
3.3 Differential Approximation	29
4. COMPARISON OF THREE-DIMENSIONAL AND ONE-DIMENSIONAL TRANSPORT	36
4.1 Adequacy of Angular Resolution	36
4.2 Comparison Calculations	38
5. CONCLUSIONS	50
6. REFERENCES	51
7. APPENDIX A - Mathematical Developments	53

1. INTRODUCTION

The analysis of the coupled radiative transport which occurs in the shock layer surrounding a vehicle entering a planetary atmosphere at extreme velocities is complicated by two factors. One of these factors is that the radiant energy transport is determined by an integral of the monochromatic intensity over the spectrum; an integral requiring treatment of complex absorption processes. Despite its complexity, a number of investigators (Ref. 1-6) have successfully solved the spectral integration problem using a realistic frequency dependence of the spectral absorption coefficients. The second complicating factor is that the radiant energy transport also requires a three-dimensional integration of the total intensity over all directions. Aside from being complicated numerically, this solid angle integration changes the mathematical character of the basic flow equations. Without radiation, the gasdynamic equations in the thin shock layer limit (a limit which is valid for a wide variety of vehicle configurations) are parabolic (Ref. 7). This provides a tremendous simplification by permitting the flow field to be calculated using a forward integration procedure starting at the vehicle stagnation point. When coupled radiation transport is included in the analysis, the equations become elliptic and the thin shock layer simplification is lost.* Primarily because of the desire to retain the simplicity of a parabolic system, all

* These comments do not apply to the time dependent method of Callis (Ref. 5) for which the equations are always hyperbolic in the time marching direction. However, the time dependent method is more sensitive than the steady state methods to the computational burden of a three-dimensional solid angle integration as the entire flow field must be solved numerous times. Hence the time dependent methods also resort to approximate treatment of the angular integration.

previous studies of coupled radiating flow over blunt bodies which consider detailed spectral transport (and most of those which consider simplified grey gas models) have reduced the radiative transport to a one-dimensional level. Mathematically this is accomplished by retaining only the normal component of the radiative flux (i.e., normal to the body or shock depending on the coordinate surface being used); the component of the radiative flux in the streamwise direction being neglected, e.g. Ref. 8.

It is the purpose of this study to establish the accuracy of this one-dimensional integration. We have used numerical methods to perform the required three-dimensional spatial integration, thus obtaining essentially exact values for the radiative flux and its divergence. We then tested three one-dimensional transport models against these three-dimensional numerical solutions. The one-dimensional models were the tangent slab and the full- and half-range differential approximations.

This study evaluating radiative transport approximations is oriented to the problem of entry vehicle radiative heating. Thus we have employed the following ground rules. A blunted cone configuration typical of entry bodies was considered. The distribution of thermodynamic variables in the shock layer about the body were taken from a fully coupled solution of the flow of a radiating gas about a blunt body.* In this manner a realistic flow field was used in the evaluation. In evaluating the radiative transport we used a simplified three-group model for continuum-only air radiation. This model has been employed by IMSC in other coupled flow studies and has been established as a reasonably accurate treatment for continuum-only transport.

*The flow field solution was one kindly provided by Mr. Lin Callis of NASA Langley Research Center. This solution employed a multi-group grey gas absorption coefficient model (Ref. 5) thus accounting for the essential radiative characteristics of high temperature air.

Moreover, the bands display a desirable variation in optical depth (for the particular flow field considered) with the first group being optically thin, the second group having intermediate optical depth and the third group being optically thick.

A series of numerical calculations were performed for the basic blunted cone shock layer configuration. The results of these calculations show that the one-dimensional approximations to the radiative flux divergence is accurate to within a few percent in determining the total energy lost by the shock layer, i.e., as measured by the integral of the flux divergence from shock to body. Locally, in regions where the flux divergence is small the percentage error can be appreciable; however, these regions have little effect on the total energy loss. This conclusion is of fundamental importance as it demonstrates that one-dimensional methods can be employed in the coupled radiating flow calculation with assurance that the resulting thermodynamic field is correct. In terms of calculating the surface flux, the one-dimensional approximations introduce the largest errors near the stagnation point where the errors are about 15%. The source of these errors is the slab-like geometric representation inherent in all one-dimensional models. On the conical afterbodies where the shock layer geometry is much more slab-like, the errors are reduced below 10%. Finally, it is found that for both the radiative flux and its divergence, the tangent slab approach generally provides the most accurate results when compared with the differential approximation methods.

2. THREE-DIMENSIONAL CALCULATIONS

2.1 GEOMETRIC CONSIDERATIONS

The body and shock shape combination is shown in isometric view in Fig. 1. In analyzing the various geometric constraints on the angular integration problem we elected to simplify the analysis by restricting the body and shock shapes to those describable as a general conic section. However, we allow the describing equations to be given in two segments with the two segments tangent at the common point. Letting r and z be the radial and axial variables in a cylindrical coordinate system, then the general conic section equation is*

$$r^2 = 2a(z - \delta_0) - b(z - \delta_0)^2 \quad (1)$$

where a subscript on a , b , and δ_0 differentiates between the body (b) and shock (s). Again, we allow both body and shock shape to be represented by two equations of the type shown above with the tangent point denoted by subscript t .

The flow field solution which was provided by Callis was that for a 45° hemispherically blunted conical body. For such a body, Eq. (1) is an exact representation. The body and our approximation, via Eq. (1), to the shock it supports for the flight conditions analyzed (the details of the flight condition and resulting flow field will be discussed in Subsection 2.4) is shown in Fig. 2. Table 1 lists the coefficients of Eq. (1) for body and shock along with the actual and our approximation to the r , z coordinates

* All lengths are scaled to the body hemispherical nose radius and δ_0 physically represents the shock layer thickness at zero.

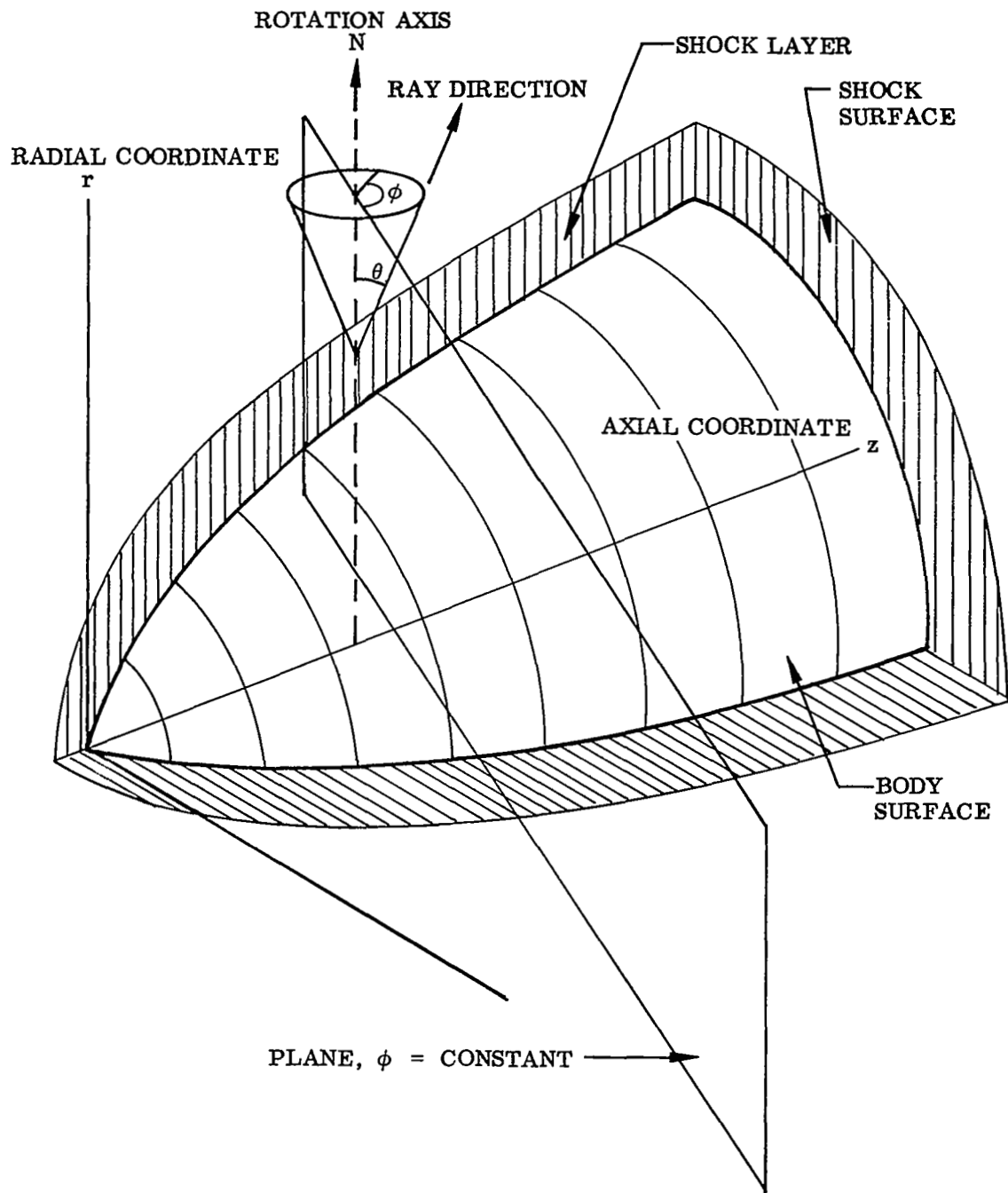


Fig. 1. - General Configuration of Shock Layer
 and the θ, ϕ Coordinates for Ray Tracing

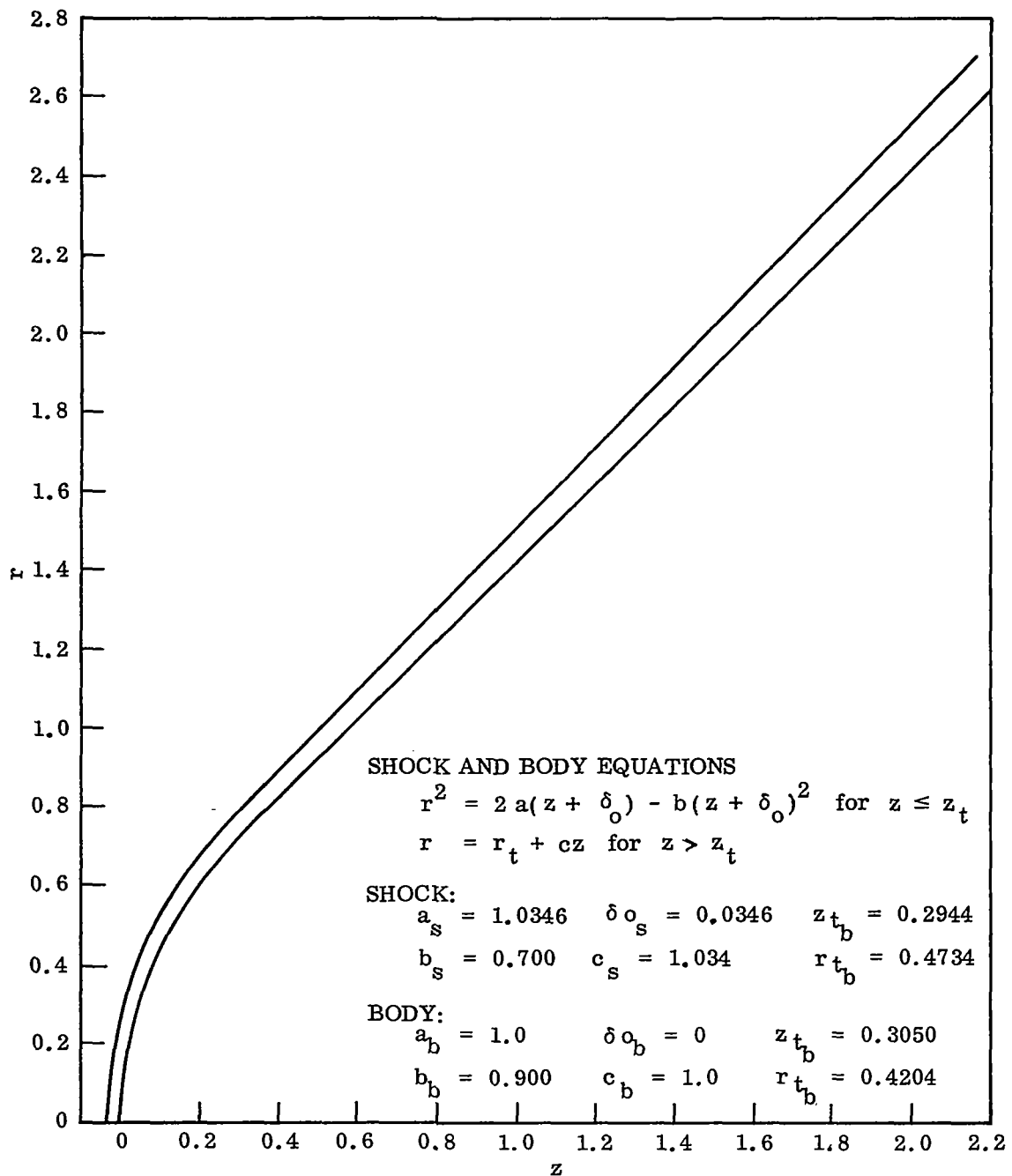


Fig. 2. Shock & Body Shapes

of the body and shock.*

Table 1 - Body and Shock Shapes
From Callis' Calculation

<u>Shock</u>			<u>Body</u>		
$a_s = 1.0346; b_s = .7000; c_s = 1.034$			$a_b = 1.000; b_b = .9000; c_b = 1.000$		
$\delta_{o_s} = .0346; z_{t_s} = .2944; r_{t_s} = .4734$			$\delta_{o_b} = 0; z_{t_b} = .3050; r_{t_b} = .4204$		
z	r_{Callis}	$r_{\text{Calc.}}$	z	r_{Callis}	$r_{\text{Calc.}}$
-.0346	0	0	0	0	0
-.010	.306	.302	.045	.296	.297
.139	.589	.583	.175	.565	.568
.337	.824	.822	.371	.791	.791
.548	1.038	1.040	.583	1.003	1.003
1.108	1.610	1.619	1.149	1.569	1.569
2.145	2.694	2.691	2.209	2.629	2.629

From Table 1 we observe that Eq. (1) fits both the exact body and shock configurations quite well, with the maximum difference between exact and analytic approximation to the radial coordinate for the various axial coordinates shown being less than 1%.

In performing the angular integration we first point out that, except along the stagnation line ($r = 0$), the radiation field has no plane of symmetry. Hence, there is no preferred orientation for the coordinate system in which we evaluate the radiation field. Since we are interested in obtaining fluxes normal to and parallel to the local body tangent, it might seem advantageous to use such a body oriented system. However, in a body oriented coordinate system, it is quite difficult to obtain the body-shock shape geometry for a general

* Apparently, the body studied by Callis is not precisely a spherical nose. Hence, we adjusted the coefficient b to obtain the values shown in Table 1.

azimuthal plane. (Only when the azimuthal plane lies in a meridional plane does the geometry become simple.) Hence, we have elected to perform the angular integrations using the coordinate system sketched in Fig. 1. That coordinate system is described by azimuthal planes which rotate about an axis parallel to the radial coordinate. Within each plane, the radiant intensity is evaluated as a function of angle measured with respect to the rotation axis. Hence, in this coordinate system, we evaluate the components of the net flux in the r and z directions.

The geometry picture will be clarified by reference to Figs. 3, 4, and 5.* In Fig. 3 we display a view looking down along the rotation axis of Fig. 1, i.e., a "top" view. We can see that the various azimuthal planes are defined by the condition $\varphi = \text{constant}$. The plane perpendicular to the axial coordinate z is defined to be $\varphi = 0$. Before leaving Fig. 3, note that L is the distance from the rotation axis measured along a generator of the φ plane. Now we consider Fig. 4, which shows the view in the plane $\varphi = \text{constant}$. Note that for a general value of φ , the body and shock shape are not axisymmetric. Indeed, for φ greater than the asymptotic shock and body cone angles, these surfaces are not closed. In the view offered by Fig. 4, we can see clearly the definition of the elevation angle θ . Together, the angles φ, θ define a direction (i.e., ray) along which the radiant intensity is determined. The distance along a given ray is defined by the variable s . Because of the nonsymmetry in the plane $\varphi = \text{constant}$, it is necessary to evaluate the radiant intensity $I(\theta, \varphi)$ over the range $0 \leq \theta \leq 2\pi$. Of course, this means that the total 4π steradiancy is described by rotating the azimuthal

* In Figs. 3, 4, and 5, the scale of the shock layer thickness is greatly magnified for ease of interpretation.

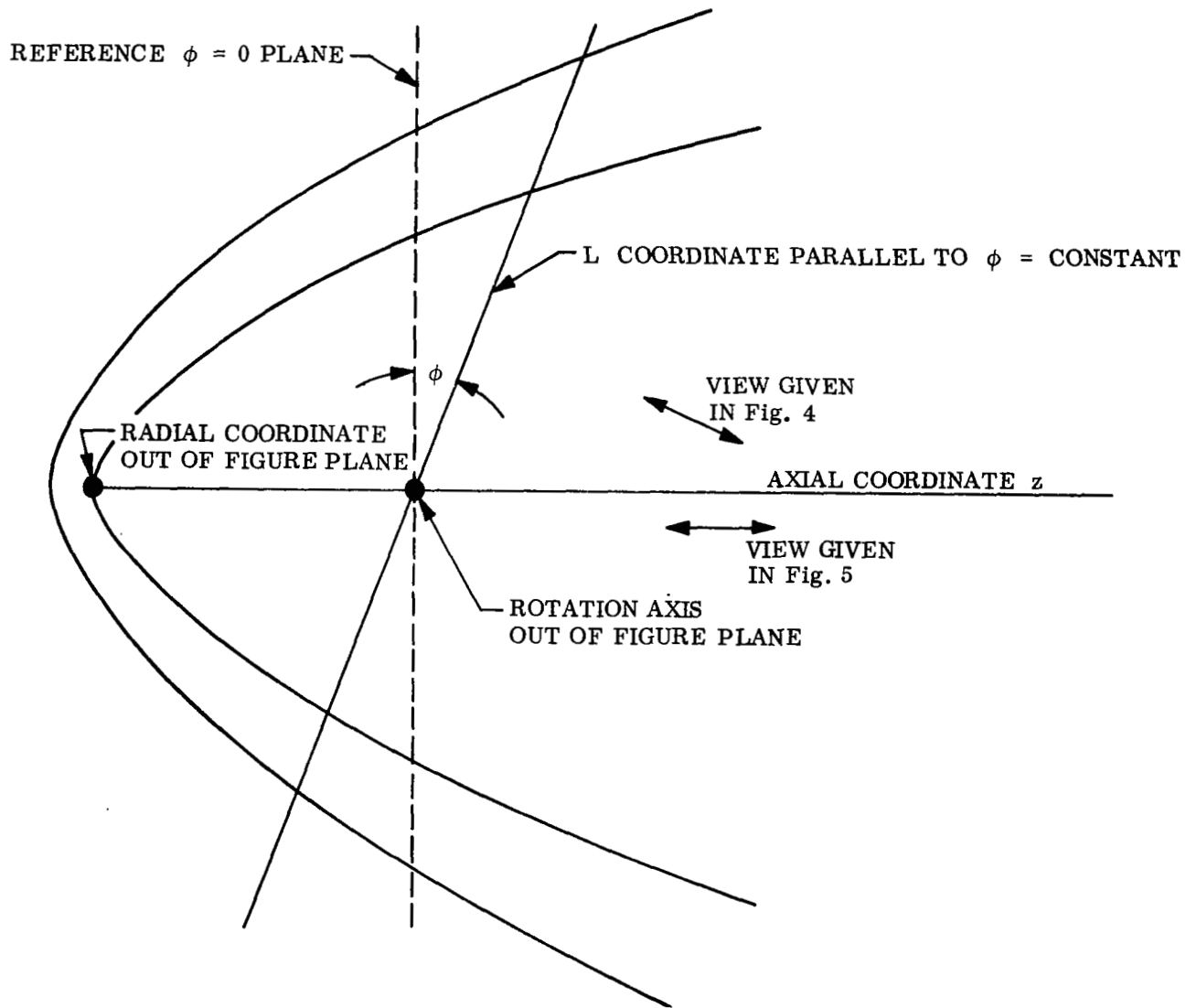


Fig. 3. - Top View Along the ϕ Rotation Axis Showing Geometric Position of ϕ Constant Planes

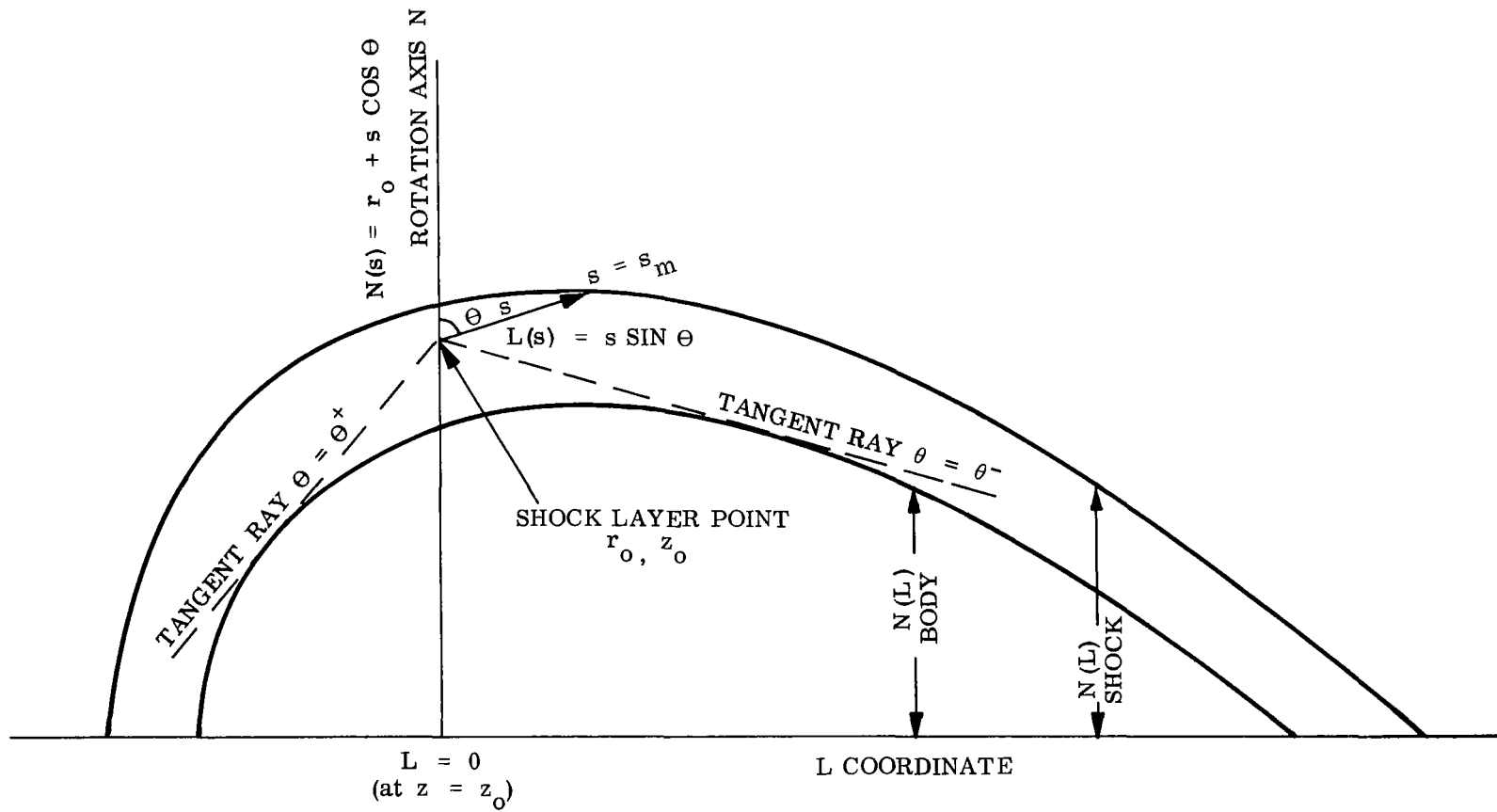


Fig. 4. - View in a ϕ Plane Showing Geometric Position of θ Constant Ray

plane over the range $0 \leq \varphi \leq \pi$. At this point we should observe from Fig. 3 that there is a bilateral symmetry about the z-axis so that it is only necessary to perform the numerical calculation over the range $0 \leq \varphi \leq \pi/2$ and, subsequently, double the resultant r, z flux components.

Returning to the Fig. 4 and the θ variable, there are two limiting values of θ designated as θ^- and θ^+ , which describe that portion of θ space occupied by the body. These limiting angles are φ dependent. For values $\theta^+ \leq \theta \leq \theta^-$, a given ray is bounded by the shock surfaces whereas, for $\theta^- \leq \theta \leq \theta^+$, the body is the limiting surface. Hence, the intensity undergoes a discontinuity at θ^- and θ^+ , and we have anticipated this behavior in establishing the angular integration mesh. Analytical equations were developed for determining θ^- and θ^+ as a function of φ .*

In order to evaluate the radiant intensity along a given φ, θ direction, it is necessary to relate the location φ, θ, s along a ray, first to r, z coordinates, and subsequently, to the body oriented coordinate in which the flow field is available. From Figs. 3 and 4, it is apparent that the z component along a ray is simply

$$z(s, \theta, \varphi) = z_0 + s \sin\theta \sin\varphi \quad (2)$$

However, we emphasize that while the rotation axis N is aligned with the radial axis r, once the point is away from the N axis (i.e., $s \neq 0$), the projection on the N axis is not the radial coordinate $r(s, \theta, \varphi)$. (The exception is when $\varphi = 90^\circ$, for then the φ plane coincides with a meridional plane.) This condition is clarified with the aid of Fig. 5 which is the view described in Fig. 3, a view taken through the plane normal to the z-axis. Fig. 5 shows

*For convenience, all detailed mathematical developments are collected in Appendix A.

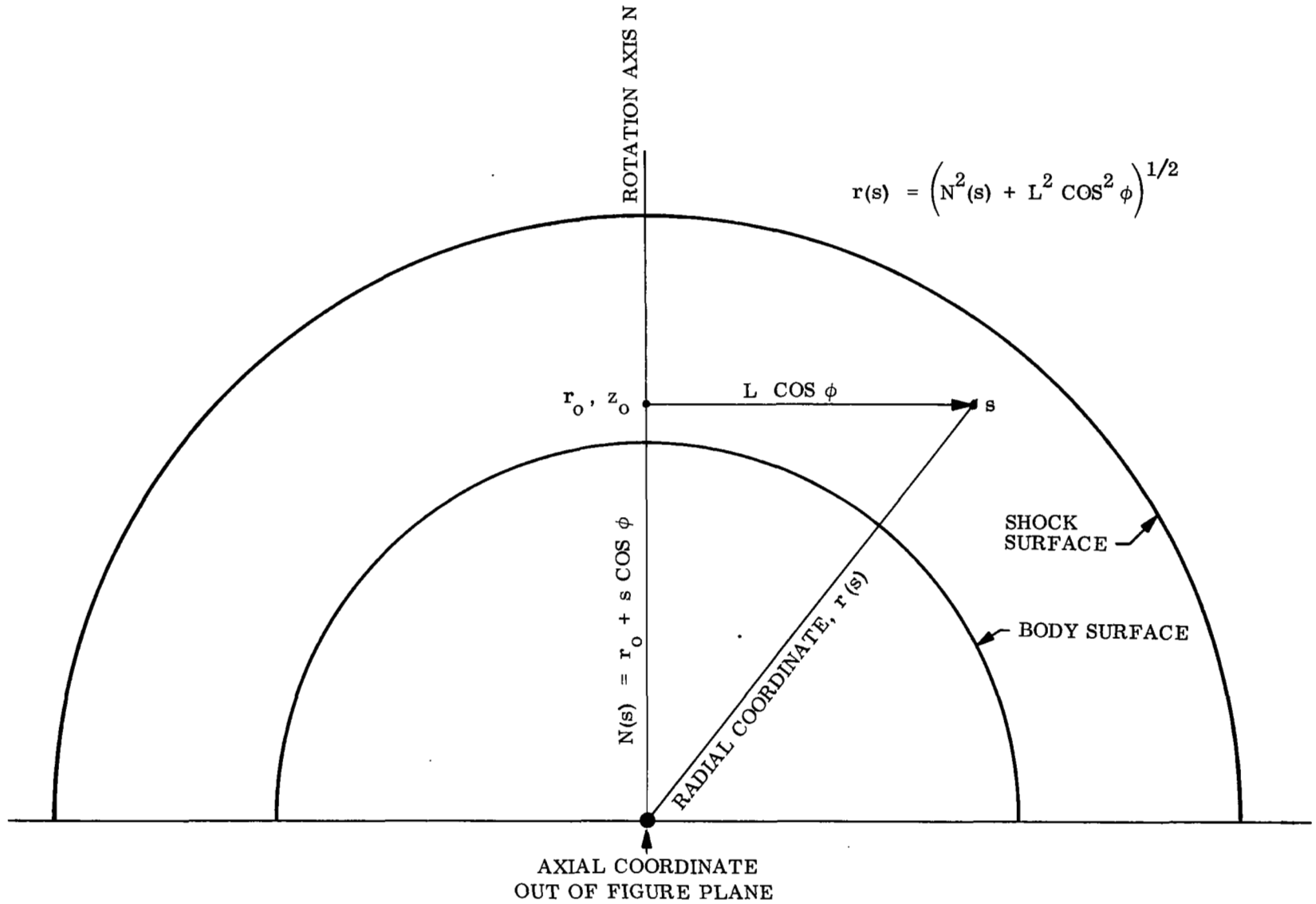


Fig. 5. - View Perpendicular to Symmetry Axis Showing Construction of Local Radial Coordinate Value

that the radial coordinate desired is:

$$r^2(s, \theta, \varphi) = (r_0 + s \cos \theta)^2 + (s \sin \theta \cos \varphi)^2 \quad (3)$$

The bounding values of the path length s_m can be obtained in a straightforward manner by observing that at either the shock or body surfaces, the radial coordinate given by Eq. (3) must equal that given by Eq. (1) with, in Eq. (1), the axial coordinate given by Eq. (2). These three equations combine to yield a quadratic equation for $s_m(\theta, \varphi)$ as detailed in Appendix A. There is one condition for which the equations for s_m admit no solution. Physically this reflects the fact that the shock and body are conical beyond their respective tangent points and, in addition, they diverge. That is, the asymptotic shock angle is larger than the asymptotic body angle. Then, for any value of $\varphi > \varphi^*$ where

$$\varphi^* = \tan^{-1}\left(\frac{1}{c_s}\right) \quad , \quad (4)$$

with c_s the slope of the shock in the r, z coordinate system, the shock surface does not close. Hence, when $\varphi > \varphi^*$ there is a range of θ values for which a given ray will not intersect the body or shock. These are θ values in range $\theta^* \leq \theta \leq \theta^-$ with

$$\theta^* = \cot^{-1}(c_s^2 \sin^2 \varphi - \cos^2 \varphi)^{\frac{1}{2}}$$

For θ values which fall in this range, $s_m = \infty$. Of course, the pathlength integration cannot be carried to infinity and we set $s_m = 10$ as a limit for these conditions.

As we march along a given ray, Eqs. (2) and (3) provide the local r, z coordinates. The shock layer flow field variables are specified in terms of boundary layer coordinates fixed on the body with x being the distance along

the body surface measured from the stagnation point and y the distance normal to the body. The relations between the $r, z,$ and x, y coordinate system is shown in Fig. 6. The key variable is z_b , the value of the axial coordinate from which a body normal will pass through the r, z point in question. However, since we do not know the direction of the body normal until we determine z_b itself, the procedure requires an iterative solution for z_b . Using the z_b value obtained from the previous pathlength point, this iterative evaluation proceeds quite rapidly. Of course, when z_b is such that it is on the conical portion of the body this iterative procedure is unnecessary. Having determined z_b , the x coordinate is obtained from

$$x = \int_0^{z_b} \left[1 + \left(\frac{dr}{dz} \right)^2 \right]^{\frac{1}{2}} dz \quad (6)$$

with dr/dz calculated from Eq. (1). The y coordinate may be written down directly as, cf. Fig. 6,

$$y = \frac{(z_b - z_0 - s \sin\theta \sin\varphi)}{\sin\delta_b} \quad (7)$$

where δ_b is the angle between the body normal at $z = z_b$ and the r direction.

Equation (1) provides a good approximate description of the body and shock shape. However, the shock thickness is obtained by a subtraction process and downstream of the tangent point, where the shock has a slight inflection, errors of the order of 10% in shock layer thickness result. Such an error cannot have much of an effect on the geometric character of the radiation field (i.e., the error does not impact critically on the primary objective of evaluating the one-dimensional radiation transport model). Indeed, there is no "error" if we view our results as specific to the particular shock-body configuration offered by Eq. (1), and having generality in the broad

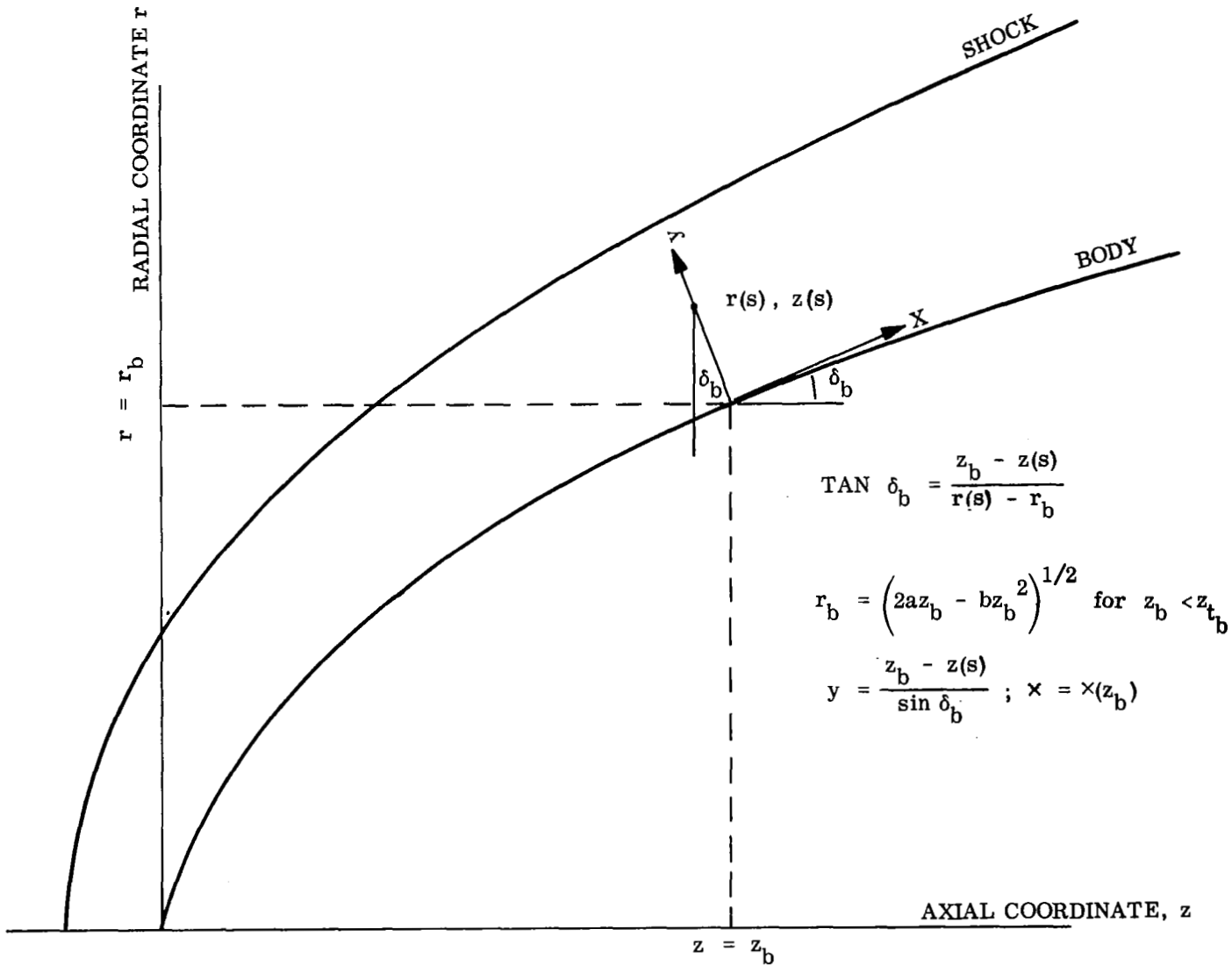


Fig. 6. - View in a Meridional Plane Showing Geometric Relation Between r, z Coordinates with x, y Body Coordinates

sense that these results are applicable to the characteristic shock layer geometry. However, we do not wish to introduce extrapolation errors in applying the available shock layer flow field data. Accordingly, we use the shock layer data in a normalized form with the flow field data given as a function of $y/\delta(x)$ where $\delta(x)$ is the local shock layer thickness. However, in translating these normalized distributions back to the physical coordinate, we use $\delta(x)$ from our approximate shock and body shape relations, Eq. (1), rather than the shock layer thickness provided by Callis' solution. The appropriate value for $\delta(x)$ is that evaluated at the x-coordinate given by Eq. (6). As shown in geometric sketch of Fig. 6, we obtain the r, z coordinates of the intersection of the body normal with the shock (denoted as r_s, z_s) from which

$$\delta(x) = y(r_s, z_s) = \frac{r_s - r_b}{\cos \delta_b} \quad (8)$$

This completes the description of the methods used to determine the required geometric relations for locating points along a ray in an arbitrary θ, φ direction.

2.2 ANGULAR INTEGRATIONS

Referring back to Fig. 1, we note that the net radiative flux vector can be described most conveniently by its components in the r, z directions. For the cylindrical r, z coordinate system, the third coordinate is the circumferential direction ψ measured about the symmetry axis z . However, the flow component in this direction F_ψ is zero. In general, the flux component F_n in the direction of the unit normal \hat{n} is (Ref. 9)

$$F_n = \int_{\Omega=4\pi} \hat{n} \cdot \vec{s} I(s) d\Omega \quad (9)$$

where \vec{s} specifies the local direction of the ray along which the intensity is given. To find the desired flux components consider the sketch below which expands the N, θ, ϕ coordinate system (shown in Fig. 1) in which we are evaluating the intensity.

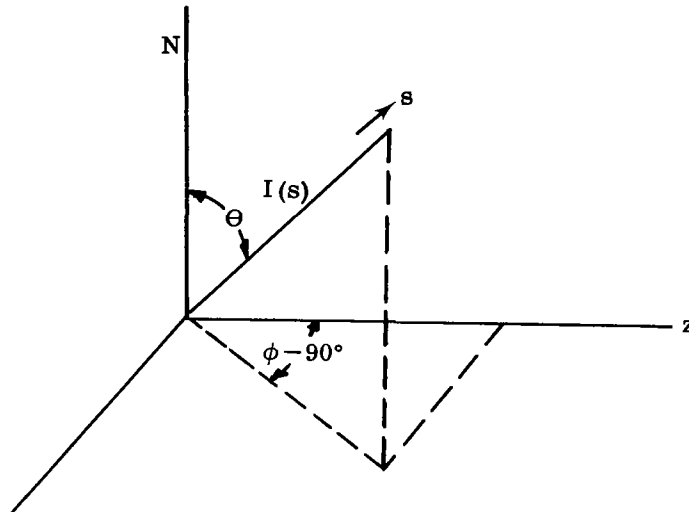


Fig. 7. - The N, θ, ϕ Coordinate System

In the N, θ, ϕ system, the increment of solid angle is

$$d\Omega = |\sin\theta| d\theta d\phi \quad (10)$$

We note the absolute value on the $\sin\theta$ term in Eq. (10). This requirement stems from the definition of incremental solid angle (ratio of incremental area to the square of the separation distance) which demands that $d\Omega$ always be positive. For the plane parallel problems the reader is probably familiar with, the θ variable has the range $0 \leq \theta \leq \pi$ while ϕ is swept over 2π . However, recall that the conditions on our problem require the opposite limits, i.e., $0 \leq \theta \leq 2\pi$ and $0 \leq \phi \leq \pi$. Since $\theta > \pi$; $\sin\theta < 0$, and hence we must redefine $d\Omega$ as $d\Omega = -\sin\theta d\theta d\phi$ when $\pi \leq \theta \leq 2\pi$.

From a computational point it is simpler to use the definition of Eq. (10).

For the flux component in the radial direction (keeping in mind that N and r are parallel so that the unit vector is taken along the N axis), we note that $\hat{n} \cdot \vec{s} = \cos\theta$. This is the usual result given for plane-parallel geometries in which the angular coordinates are measured about the normal to the surface whose flux component is to be determined. Hence, we can write

$$F_r(r_o, z_o) = \int_0^\pi \int_0^{2\pi} I_{r_o, z_o}(\theta, \varphi) \cos\theta |\sin\theta| d\theta d\varphi \quad (11)$$

For the flux component in the axial direction (i.e., where the unit vector is in the z direction) $\hat{n} \cdot \vec{s} = \sin\theta \sin\varphi$. This is the component of the flux normally not calculated in plane-parallel geometries since it is identically zero. However, in our case we have

$$F_z(r_o, z_o) = \int_0^\pi \int_0^{2\pi} I_{r_o, z_o}(\theta, \varphi) \sin\theta |\sin\theta| \sin\varphi d\theta d\varphi \quad (12)$$

In order to decompose the flux into the desired components in the body oriented system, we note from the following sketch:

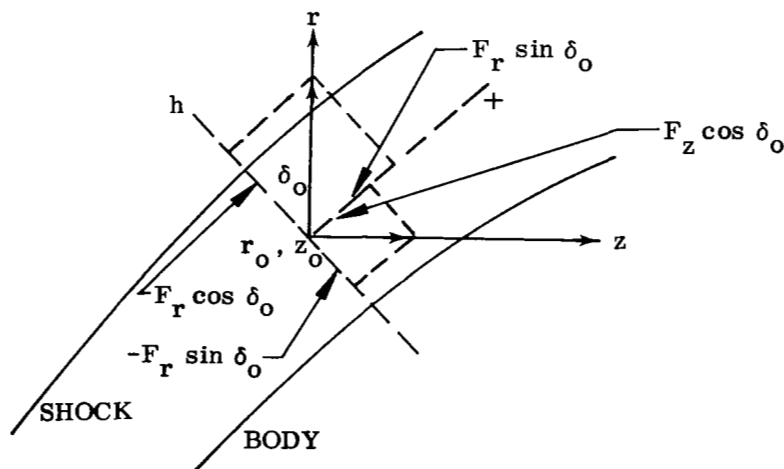


Fig. 8. - Transformation of Flux Components

that

$$F_x = F_z \cos \delta_o + F_r \sin \delta_o \quad (13)$$

$$F_y = F_r \cos \delta_o - F_z \sin \delta_o \quad (14)$$

where δ_o is the angle defined by the r axis and the body normal which passes through the r_o, z_o point of interest. From Eq. (14) we see that F_y is obtained via a subtraction process. Recall from our earlier discussion on determination of the ray boundaries (i.e., $\theta = \theta^+$ and $\theta = \theta^-$) that rays which are nearly parallel to the body are not terminated, for certain φ values, by either the body or shock leading to $s_m = \infty$. Since these rays are nearly parallel to the body, it is clear that they do not play an important role in determining F_y . However, due to the necessity of using a finite value of s_m , concern arose that possible errors introduced into F_r and F_z would not cancel when F_y was constructed via Eq. (14). To eliminate this possibility, F_y was obtained by an alternate method in which Eqs. (11) and (12) were substituted directly into Eq. (14) yielding the result,

$$F_y(r_o, z_o) = \int_0^{\pi} \int_0^{2\pi} I_{r_o, z_o}(\theta, \varphi) \sin\theta |\sin\theta| q(\theta, \varphi) d\theta d\varphi \quad (15)$$

$$\text{with} \quad q(\theta, \varphi) = (\cot\theta - \tan \delta_o \sin\varphi) \cos \delta_o \quad (15a)$$

We note that when θ becomes parallel to the body $q(\theta, \varphi)$ is identically zero ensuring that any errors in $I(\theta, \varphi)$ at this θ value will be cancelled by $q(\theta, \varphi)$.

The other quantity we are interested in is the flux divergence which is given by

$$\nabla \cdot F(r_o, z_o) = \frac{\partial F}{\partial y}(r_o, z_o) = \mu(r_o, z_o) \left\{ \int_{\Omega=4\pi} I_{r_o, z_o}(\theta, \varphi) d\Omega - 4\pi B(r_o, z_o) \right\} \quad (16)$$

where μ is the absorption coefficient, and B the Planck function at the point r_o, z_o of interest. Using Eq. (10), we have

$$\int I_{r_o, z_o}(\theta, \varphi) d\Omega = \int_0^\pi \int_0^{2\pi} I_{r_o, z_o}(\theta, \varphi) |\sin\theta| d\theta d\varphi \quad (17)$$

Before leaving the section on angular integrations, the mesh selected for the θ and φ variables will be discussed. There was no reason to suspect large nonuniformities in the intensity (integrated over θ) as a function of the azimuthal angle φ . Hence, a uniform φ mesh was selected. In establishing accuracy of the numerical integration scheme, calculations with $\Delta\varphi = 5^\circ$ and 10° were performed. On the basis of these calculations it was determined that $\Delta\varphi = 10^\circ$ was adequate and this value was used in the results shown later. The variation of the θ integrated intensity as a function of φ was examined and found to be quite smooth. From this a posteriori test we concluded that our original choice of a uniform φ mesh was correct.

In establishing the θ mesh, it was clear under most situations, the intensity $I(\theta, \varphi)$ would be discontinuous at $\theta = \theta^-$ and $\theta = \theta^+$. To provide for this discontinuous behavior, the θ integration was performed in terms of four quadrants. Referring to Fig. 4 we find that the angles defining the four quadrants are as tabulated below:

Quadrant	Angular Range	
	$z_o > 0$	$z_o < 0$
1	$0 \leq \theta \leq \theta^-$	$0 \leq \theta \leq \theta^-$
2	$\theta^- \leq \theta \leq \pi$	$\theta^- \leq \theta \leq \pi/2$
3	$\pi \leq \theta \leq \theta^+$	$\pi/2 \leq \theta \leq \theta^+$
4	$\theta^+ \leq \theta \leq 2\pi$	$\theta^+ \leq \theta \leq 2\pi$

In addition to performing a separate integration in each quadrant, we focus a larger number of rays in the θ regions near θ^- and θ^+ . This was accomplished by using a geometric series for $\Delta\theta$ starting with $\Delta\theta = 1^\circ$ at $\theta = \theta^-$ or θ^+ and increasing according to a specified growth rate. For the results shown, we used a growth factor of 1.05 which typically required about 150 values of θ to cover the range from 0 to 2π for each of the 10 φ planes considered. Hence, we calculated the intensity for, roughly, a total of 1500 rays. The computation time for each combined flux and flux divergence calculation was about 1 minute on IMSC's 1108 system.

2.3 GASDYNAMIC, THERMODYNAMIC AND RADIATIVE TRANSPORT PROPERTIES

It was stated in the introduction that one of the ground rules under which the study of three-dimensional transport effects was to be carried out, was that a realistic coupled radiating flow field solution would be used. IMSC was fortunate to have the cooperation of the NASA Langley Research Center in providing such a solution. Callis, using his time-dependent method (Ref. 5), calculated the flow past a 45° spherically blunt cone for the following conditions:

$$\begin{aligned}
 U_\infty &= 16 \text{ km/sec} \\
 \rho_\infty &= 4.43 \times 10^{-7} \text{ gm/cm}^3 \\
 p_s &= 1.00 \text{ atm.} \\
 R_n &= 2.34 \text{ m}
 \end{aligned}$$

As mentioned previously, the resulting body and shockwave shapes are those given by Fig. 2. Shock layer distributions of static enthalpy and pressure through the shock layer exhibited some oscillations apparently due to the numerical methods employed. These numerical oscillations were relatively

small (less than 5%) and we have simply used smoothed enthalpy, pressure profiles to determine the temperature and number density variations in the shock layer. The smoothed pressure was essentially constant across the shock layer and hence the pressure is taken as constant in the shock normal coordinate at the value immediately behind the shock. The smoothed static enthalpy profiles used in our calculation are shown in Fig. 9 for a number of body locations.

The thermodynamic and radiative transport model used was that previously developed by Chou and Blake (Ref. 8). The temperature is obtained from the simplified state relation

$$T(^{\circ}\text{K}) = 28.4 \left(\frac{\bar{h}}{R}\right)^{0.488} \quad (18)$$

where \bar{h} is the static enthalpy in erg/gm and R is the gas constant for cold air, $R = 2.86 \times 10^6$ erg/gm $^{\circ}\text{K}$. The number densities (required for the absorption coefficients) is obtained from the approximate dissociation- ionization model of Chou and Blake (Ref. 8),

$$N_a = (1-\beta)N_t \quad (19)$$

where N_a is the number of "air" atoms and N_t the total number of particles.

From the ideal gas law

$$N_t = 6.32 \times 10^{17} p/kT$$

with p in atms and kT in eV units. The quantity β in Eq. (19) takes on one of two values dependent on whether the flow is the ionization or dissociation regimes:

$$\text{if } \beta_i \geq .005 \quad \beta = \beta_i$$

$$\text{if } \beta_i < .005 \quad \beta = \beta_d$$

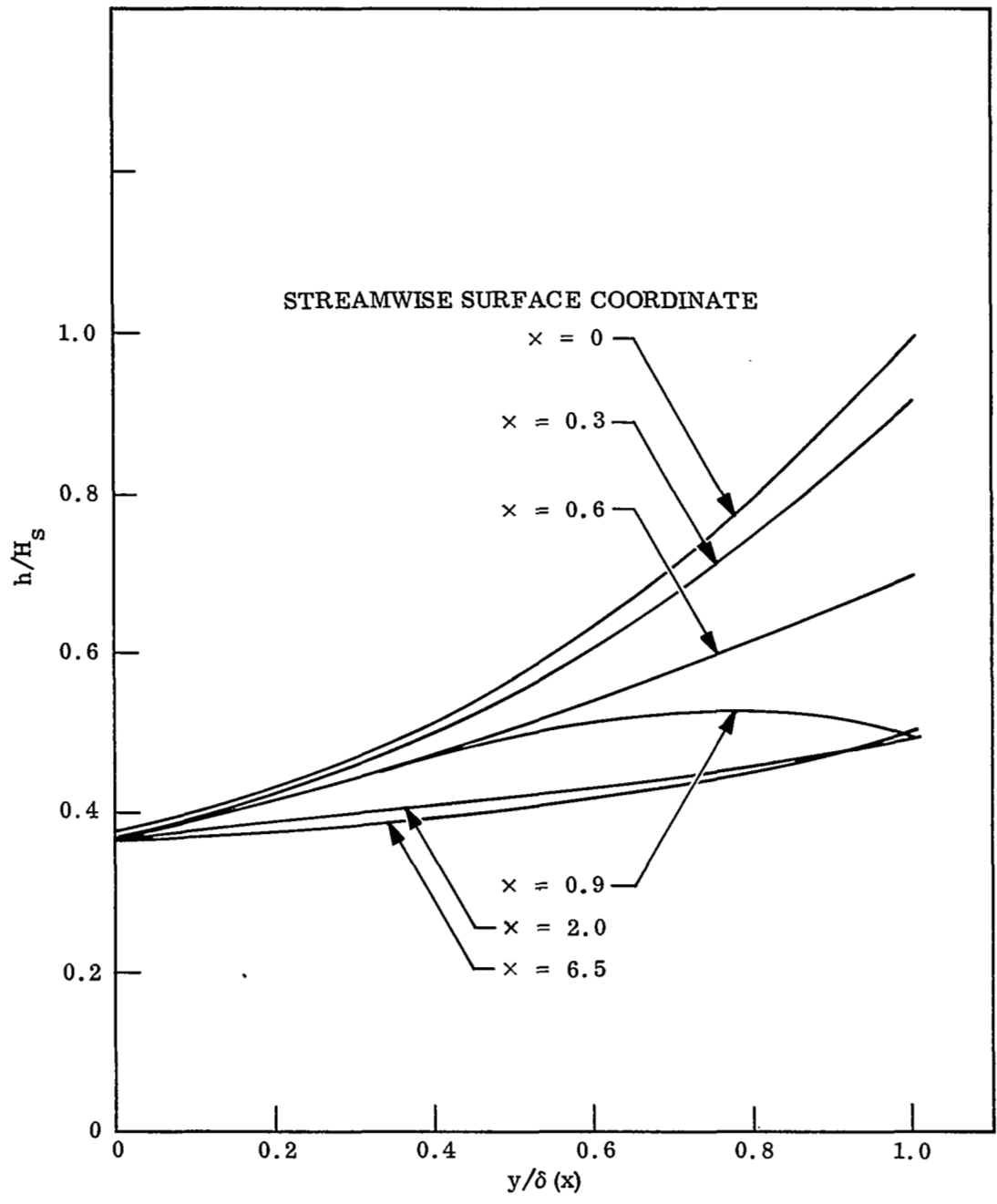


Fig. 9.- Smoothed Static Enthalpy Profiles Through the Shock Layer

where

$$\beta_i = \left\{ \frac{\frac{a_o}{p} (kT)^{5/2} e^{-14.54/kT}}{1 + \frac{a_o}{p} (kT)^{5/2} e^{-14.54/kT}} \right\}^{\frac{1}{2}} \quad (20a)$$

$$\beta_d = \left\{ \frac{a_1/p e^{-9.76/kT}}{1 + a_1/p e^{-9.76/kT}} \right\}^{\frac{1}{2}} \quad (20b)$$

and $a_o = 2.15 \times 10^4$; $a_1 = 4.28 \times 10^6$

In Eq. (20), p is in atm. and kT in eV units.

A three group piecewise grey absorption coefficient model which accounts for the continuum absorption processes in high temperature air, as developed by Chou and Blake, was employed in our calculations. The first group extends over the frequency range from $0 \leq h\nu \leq 10.8$ eV; a region of low absorption where a Planck mean absorption coefficient is valid for the shock layer thickness and pressure considered. The two high frequency groups model the weak frequency dependence of the cross sections resulting from photoionization of low lying and ground states of nitrogen and oxygen. Along with frequency averaged absorption coefficients, the transport equation requires an integral of the Planck function over each of the three frequency groups. The partial Planck integrals are listed below together with the absorption coefficients.

Group 1: $0 \leq h\nu \leq 10.8$ eV

$$\mu_1 = N_a \left\{ \frac{4.5 a_2 e^{-14.3/kT} [2.10 + kT < 0.24 + 0.0853(kT)^2 >]}{(kT)^3 \left[\frac{\pi^4}{15} - e^{-10.8/kT} \left\{ \left(\frac{10.8}{kT} \right)^3 + 3 \left(\frac{10.8}{kT} \right)^2 + 6 \left(\frac{10.8}{kT} \right) + 6 \right\} \right]} \right\} \quad (21)$$

$$B_1 = 5.04 \times 10^3 (kT)^4 \left\{ \frac{\pi^4}{15} - e^{-10.8/kT} \left[\left(\frac{10.8}{kT} \right)^3 + 3 \left(\frac{10.8}{kT} \right)^2 + 6 \left(\frac{10.8}{kT} \right) + 6 \right] \right\} \quad (22)$$

Group 2: $10.8 \text{ eV} \leq h\nu \leq 12.0 \text{ eV}$

$$\mu_2 = N_a \frac{5.16 \times 10^{-17} e^{-3.57/kT}}{(4+10 e^{-2.38/kT} + 6 e^{-3.75/kT})} \quad (23)$$

$$B_2 = 5.04 \times 10^3 (kT)^4 \left\{ e^{-10.8/kT} \left[\left(\frac{10.8}{kT} \right)^3 + 3 \left(\frac{10.8}{kT} \right)^2 + 6 \left(\frac{10.8}{kT} \right) + 6 \right] - e^{-12.0/kT} \left[\left(\frac{12.0}{kT} \right)^3 + 3 \left(\frac{12.0}{kT} \right)^2 + 6 \left(\frac{12.0}{kT} \right) + 6 \right] \right\} \quad (24)$$

Group 3: $12.0 \text{ eV} \leq h\nu \leq \infty$

$$\mu_3 = N_a \frac{[5.16 \times 10^{-17} e^{-3.57/kT} + 6.4 \times 10^{-17} e^{-2.38/kT}]}{[4+10 e^{-2.38/kT} + 6 e^{-3.57/kT}]} \quad (25)$$

$$B_3 = 5.04 \times 10^3 (kT)^4 \left\{ e^{-12.0/kT} \left[\left(\frac{12.0}{kT} \right)^3 + 3 \left(\frac{12.0}{kT} \right)^2 + 6 \left(\frac{12.0}{kT} \right) + 6 \right] \right\} \quad (26)$$

In Eqs. (21) through (26), kT is in eV, μ is in cm^{-1} , the partial Planck integral in $\text{W/cm}^2 \text{sr}$, and the constant a_2 has the values $7.26 \times 10^{-16} \text{ cm}^2 \text{eV}^2$.

3. ONE-DIMENSIONAL TRANSPORT

3.1 SOLUTION FOR THE INTENSITY

Along a given ray defined by the φ, θ directions, the intensity at the point r_o, z_o of interest is given by*

$$I_{r_o, z_o}(\varphi, \theta) = \int_0^{s_m(\varphi, \theta)} \mu[T(s), p(s)] B[T(s)] e^{-R_n \int_0^s \mu[T(s'), p(s')] ds'} ds \quad (27)$$

where μ and B are the frequency averaged properties denoted by Eqs. (21)-(26). It should be clear, then, that Eq. (27) is to be solved separately for each of the three frequency groups. In arriving at Eq. (27), we use boundary conditions which state that the inwardly directed intensity is zero at the body and shock surfaces. Rather than the transport equation in the form given by Eq. (27), a superior form for numerical computation is to rewrite Eq. (27) in terms of an emissivity function

$$E(s) = 1 - e^{-\ell R_n \int_0^s \mu(s') ds'} \quad (28)$$

where we have introduced the parameter ℓ into the exponential argument so that the emissivity function can later be used in a flux calculation. For the moment we can consider $\ell = 1$. Then, using Eq. (28), the intensity equation becomes

$$I_{r_o, z_o}(\varphi, \theta) = \frac{1}{\ell} \int_0^{E(s_m)} B(s) dE(s) \quad (29)$$

* In calculating the optical depth, the length scale R_n must be reintroduced into the pathlength integral.

Equation (29) is solved by constructing a set of pathlength values as the calculation proceeds along a given θ, ϕ direction. The geometric relations described in Appendix A specify the Δs mesh, the bounding value s_m and the relations needed to first determine $h(s), p(s)$ and subsequently the thermodynamic and radiative properties.

3.2 SLAB APPROXIMATION FOR THE FLUX

The concept of a tangent slab has been used widely in calculating the radiative flux from blunt body shock layers. In this model the shock layer geometry is replaced by a plane parallel geometry (i.e. a slab of infinite extent) in which the thermodynamic properties vary only in one direction and the variation is taken to be that occurring along the local body normal. For a plane parallel geometry, the angular integration of the intensity necessary to obtain the normal component of the flux (of course, the tangential component will be zero for such a geometry) can be performed exactly. We obtain the well known result, for the flux at the body surface, $y = 0$,

$$F_P(y=0) = 2\pi \int_0^\delta \mu [T(y), p(y)] B[T(y)] \cdot \epsilon_2 [R_n \int_0^\mu \mu(y') dy'] dy \quad (30)$$

where ϵ_2 is the exponential integral function. In arriving at Eq. (30) we again use the condition of zero inward intensity at the shock and body. In Eq. (30), the integration path is along the body normal. Again we introduce an emissivity function,

$$E_P(y) = 1 - 2\epsilon_3 [R_n \int_0^y \mu(y') dy'] \quad (31)$$

and the flux becomes,

$$F_P(y=0) = \pi \int_0^{E_P(\delta)} B(y) dE_P(y) \quad (32)$$

Finally, we note that the ϵ_3 integral can be approximated by an exponential,

$$\epsilon_3(t) = \frac{1}{2} e^{-\ell t} \quad (33)$$

In which case (dropping the subscript P)

$$F(y=0) = \left(\frac{2}{\ell}\right) \pi \int_0^{E(\delta)} B(y) dE(y) \quad (34)$$

where $E(y)$ is the emissivity function defined in terms of the exponential function given by Eq. (28). Equations (32) and (34) are two approximations for determining the radiative flux within a one-dimensional approximation. These equations for the surface flux can readily be extended to the flux at some arbitrary point y along the body normal. If we denote by a superscript $+$ the flux directed toward the shock, and by a superscript $-$ the flux directed toward the body, we have

$$F_P(y) = F_P^+(y) - F_P^-(y) \quad (35a)$$

$$F(y) = F^+(y) - F^-(y) \quad (35b)$$

where

$$F_P(y) = \pi \int_0^{E_P(y, \delta)} B(y') dE_P(y, y') \quad (36a)$$

$$F_P^+(y) = \pi \int_0^{E_P(O, y)} B(y') dE_P(y', y) \quad (36b)$$

and

$$F^-(y) = \left(\frac{2}{\ell}\right) \pi \int_0^{E(y, \delta)} B(y') dE(y, y') \quad (37a)$$

$$F^+(y) = \left(\frac{2}{\ell}\right) \pi \int_0^{E(O, y)} B(y') dE(y', y) \quad (37b)$$

We mention in advance that Eqs. (37a) and (37b) will reappear in the next subsection covering the differential approximation where particular values of l will be assigned.

Before leaving the slab approximation, we write down the one-dimensional plane slab relations for the flux divergence,

$$\nabla \cdot F_P = 2\pi\mu(y)[I^+(y) + I^-(y) - 2B(y)] \quad (38)$$

where

$$I^-(y) = \int_0^{A_P(y, \delta)} B(y') dA_P(y, y') \quad (39)$$

$$I^+(y) = \int_0^{A_P(0, y)} B(y') dA_P(y', y) \quad (40)$$

and where we have introduced a new emissivity

$$A_P(y) = 1 - \epsilon_2 \left[R_n \int_{y'}^y \mu(y'') dy'' \right] \quad (41)$$

involving another exponential integral function. If we again make the exponential approximation

$$\epsilon_2(t) = - \frac{d\epsilon_3(t)}{dt} = \frac{l}{2} e^{-lt} \quad (42)$$

then we can express the flux divergence directly in terms of F^+ and F^- as given by Eq. (37). We have

$$\nabla \cdot F(y) = \mu(y) \{ l[F^+(y) + F^-(y)] - 4\pi B(y) \} \quad (43)$$

3.3 DIFFERENTIAL APPROXIMATION

3.3.1 Full-Range Formulation

As given by Vincenti and Kruger, the equations for the full-range differential approximation are

$$\nabla \cdot \mathbf{F} = -\mu(U - 4\pi B) \quad (44)$$

$$\nabla U = -3\mu F \quad (45)$$

where U is the integrated intensity

$$U = \int_{\Omega=4\pi} I d\Omega \quad (46)$$

Equation (44) is the exact statement of the radiant energy conservation law. Equation (45) follows from the Milne-Eddington approximation, relating the second angular moment of the intensity to the zeroth moment. The important point to note is that the Milne-Eddington approximation becomes exact if the intensity is isotropic over half-space (Ref. 11); this half-space being defined in terms of an arbitrarily oriented planar surface. If this condition of half-space isotropy holds, then the net radiative flux will be perpendicular to the defining surface. From these statements we can gain some insight into the general applicability of the differential approximation. It is well known that the differential approximation is accurate in planar geometries. For a planar problem the radiation field is nearly isotropic in half-space. Then we can expect for a three-dimensional system that the differential approximation will be valid if the problem has a local one-dimensional character with respect to any planar surface, not necessarily a coordinate surface.

As noted in the introduction, the equations representing the general differential approximation are simplified to a one-dimensional form when coupled with the flow equations. This is accomplished by the substitution,

$$\nabla \cdot \mathbf{F} = \frac{\partial F}{\partial y}$$

$$\nabla U = \frac{\partial U}{\partial y}$$

so that Eqs. (44) and (45) become

$$\frac{\partial F}{\partial y} = -\mu(U - 4\pi B) \quad (47)$$

$$\frac{\partial U}{\partial y} = -3\mu F \quad (48)$$

To derive boundary conditions, it is first necessary to decompose the net flux into

$$F = F^+ - F^- \quad (49)$$

where F^+ is the one-sided flux moving into the gas and F^- is the one-sided flux moving into the wall at the boundary $y = 0$. If the wall has an emissivity ϵ then at $y = 0$.

$$F^+ = \epsilon\pi B(T_w) + (1-\epsilon)F^- \quad (50)$$

We can similarly decompose the integrated intensity,

$$U = U^+ + U^- \quad (51)$$

Assuming the wall to be diffuse, the integrated intensity entering the gas is diffuse so that

$$U^+ = 2F^+ \quad (52)$$

In order to close the system, it is necessary that we specify additional information at the boundary relating the half-range integrated intensity with the half-range flux. The fact that the boundary conditions require an additional approximation beyond that required elsewhere for the differential approximation involving the zeroth and first moments is often overlooked. Consistent with the assumption of half-range isotropy used within the gaseous medium to relate the second and zeroth moments, we assume

$$U^- = 2F^- \quad (53)$$

Combining Eqs. (49)-(53), we arrive at

$$U + \frac{2(2-\epsilon)}{\epsilon} F = 4\pi B(T_w) \quad (54)$$

and for a cold, black wall ($T_w = 0$, $\epsilon = 1$) we have

$$\text{at } y = 0 \quad U + 2F = 0 \quad (55)$$

Similar arguments at the shock boundary (which is also effectively a cold black wall) lead to

$$\text{at } y = \delta \quad U - 2F = 0 \quad (56)$$

Equations (47) and (48) subject to the split boundary conditions given by Eqs. (55) and (56) form the full range differential approximation.

3.3.2 Half-Range Formulation

As an alternative to Eqs. (44) and (45), one can consider the differential approximation applied to the one-sided fluxes and intensities as defined by an arbitrary plane surface (Ref. 11). For a one-dimensional approximation, the rational choice for this "symmetry" plane is one tangent to the body at the local point of interest. This is the components F^+, F^- and U^+, U^- defined by Eqs. (49) and (51). The half-range equations are

$$\frac{dF^{+,-}}{dy} = \pm \mu (\pi B - l^{+,-} F^{+,-}) \quad (57)$$

where

$$l^{+,-} = \frac{\int I d\Omega}{2\pi \int I \vec{\Omega} d\Omega} \quad (58)$$

The defining equation for $l^{+,-}$ is evaluated for each half-space range. If we make the further assumption that the intensity is isotropic in each half-space, then

$$l^+ = l^- = l = 2 \quad (59)$$

Combining the two forms of Eq. (57) with Eq. (49) we arrive at

$$\frac{d^2 F}{\mu^2 dy^2} = \frac{4\pi}{\mu} \frac{dB}{dy} + l^2 F \quad (60)$$

In terms of the half-range formulation, we can write down directly the boundary conditions. At the body surface we have

$$F^+ = \frac{\epsilon\pi B(T_w) + (1-\epsilon)F^-}{(2-\epsilon)}$$

and for a cold black wall ($T_w = 0$, $\epsilon = 1$), we have

$$\text{at } y = 0 \quad F^+ = 0 \quad (61)$$

and similarly, at the shock, we have

$$\text{at } y = \delta \quad F^- = 0 \quad (62)$$

3.3.3 Solution to the Differential Approximation

With a little manipulation, Eqs. (47) and (48) can be combined into a form identical to Eq. (60). Then, defining an optical depth,*

$$\tau = \int_0^y \mu dy' \quad (63)$$

we can write the general equation for the differential approximation as

$$\frac{d^2 F}{d\tau^2} - l^2 F - 4\pi \frac{dB}{d\tau} = 0 \quad (64)$$

where $l = \sqrt{3}$ for the full range formulation and $l = 2$ for the half-range formulation. Using the standard method of variation of parameters, the solution to Eq. (64) is

$$F = c_0 e^{-l\tau} + c_1 e^{l\tau} + \psi_1(\tau) + \psi_2(\tau) \quad (65)$$

*For our three-group air radiation model, the differential approximation is to be solved for three separate grey flux contributions.

where

$$\Psi_1(\tau) = 2\pi \int_0^{\tau} B(\tau') e^{-\ell(\tau-\tau')} d\tau' \quad (66)$$

$$\Psi_2(\tau) = 2\pi \int_0^{\tau} B(\tau') e^{-\ell(\tau'-\tau)} d\tau' \quad (67)$$

In order to apply the boundary conditions, we solve for the integrated intensity from Eq. (47) (in optical coordinates) and obtain

$$I = \ell [c_0 e^{-\ell\tau} - c_1 e^{\ell\tau} + \Psi_1(\tau) - \Psi_2(\tau)] \quad (68)$$

Applying the boundary conditions given by Eqs. (55) and (56)*, we arrive at

$$c_0 = -\alpha_0 c_1 \quad (69)$$

$$c_1 = \frac{-e^{-\ell\tau_s}}{(1-\alpha_0^2 e^{-2\ell\tau_s})} [\Psi_2(\tau_s) + \alpha_0 \Psi_1(\tau_s)] \quad (70)$$

where $\tau_s = \tau(y=\delta)$, the optical depth of the entire layer and

$$\alpha_0 = (2-\ell)/(2+\ell) \quad (71)$$

At this point it is convenient to relate the integrals Ψ_1 and Ψ_2 to the one-sided fluxes F^+ and F^- . Comparing Eqs. (37a) and (37b) with Eqs. (66) and (67) we find,

$$\Psi_1(\tau) = F^+(\tau) \quad (72)$$

$$\Psi_2(\tau) - e^{-\ell(\tau_s-\tau)} \Psi_2(\tau_s) = -F^-(\tau) \quad (73)$$

Then combining the equations for c_0, c_1 with Eqs. (72) and (73) into Eq. (65) we arrive at

* Recall that these boundary conditions were derived using half-range fluxes, hence, they apply for either the full-range or half-range formulations. In other words, Eqs. (55) and (56) are equivalent to Eqs. (61) and (62).

$$\begin{aligned}
F = & [F^+(\tau) - F^-(\tau)] + \frac{F^-(0)}{1-\Gamma} \alpha_o e^{-\ell\tau} [1 - \alpha_o e^{-2\ell(\tau_s - \tau)}] \\
& - \frac{F^+(\tau_s)}{1-\Gamma} \alpha_o e^{-\ell(\tau_s - \tau)} [1 - \alpha_o e^{-2\ell\tau}]
\end{aligned} \tag{74}$$

and where

$$\Gamma = \alpha_o^2 e^{-2\ell\tau_s} \tag{75}$$

Although Eq. (74) seems somewhat complicated, the flux has been written out in this manner to avoid taking differences in the exponentially large integrals $\Psi_1(\tau)$ and $\Psi_2(\tau)$. Note that for the half-range formulation, $\ell = 2$, $\alpha_o = 0$, and we obtain the net flux as simply the difference of the positive and negative components. Even for the full range formulation $\alpha_o = .072$, and hence, the flux differs only slightly from the value given by the first term in Eq. (74). Of course, in the full-range formulation, $F^+(\tau)$ and $F^-(\tau)$ differ from these same quantities evaluated under the half-range formulation since the exponential arguments differ in these two approaches.

Finally, we can differentiate Eq. (74) and arrive at the flux divergence expression

$$\begin{aligned}
\frac{dF}{dy} = \mu(y) \left\{ \ell[F^+(y) + F^-(y)] + \frac{\ell F^-(0) \alpha_o e^{-\ell\tau}}{1-\Gamma} [1 + \alpha_o e^{-2\ell(\tau_s - \tau)}] \right. \\
\left. + \frac{\ell F^+(\tau_s) \alpha_o e^{-\ell(\tau_s - \tau)}}{1-\Gamma} [1 + \alpha_o e^{-2\ell\tau}] - 4\pi B \right\}
\end{aligned} \tag{76}$$

4. COMPARISON OF THREE-DIMENSIONAL AND ONE-DIMENSIONAL TRANSPORT

4.1 ADEQUACY OF ANGULAR RESOLUTION

In order to use the three-dimensional calculation of the flux and flux divergence as a standard against which the validity of the various one-dimensional model will be judged, it was first necessary to establish the accuracy of the numerical methods used in the angular integration. The accuracy of the angular integration can be established only by comparison with an exact, i.e. analytic, solution. The number of such exact solutions are limited, to the author's knowledge, to transport between concentric spherical body-shock configurations with a spherically symmetric variation in the thermodynamic properties (Ref. 12). This limits the comparisons to the stagnation region. We considered, then, the following problem for the accuracy check. The shock shape given by Eq. (1) was adjusted to be spherical with a shock layer thickness taken one-tenth the nominal value, i.e. 3.46×10^{-3} . The reason for using a very thin shock thickness was that the resulting exact solution was very closely approximated by the tangent slab result. Corrections to the slab result to yield the exact flux values could be applied in an approximate manner. Also for the comparison case, we set the shock layer temperature and pressure constant at the stagnation point shock values for the nominal $U_{\infty} = 16$ km/sec, $\rho_{\infty} = 4.10 \times 10^{-7}$ gm/cm² flight condition. The specific values were $T = 16,000$ °K; $p = 1.00$ atm. Finally, the spherical nose radius R_n was increased by a factor of 10 from the nominal 2.34 m value to retain the same physical value of the shock layer thickness δ . For a spherically concentric body-shock geometry with constant thermodynamic

properties throughout the shock layer, the surface flux at the stagnation point is (Ref. 13)

$$\begin{aligned} \frac{F}{\pi B} = & 1 - 2 \left(1 + \frac{1}{2} \frac{\delta}{R_n}\right)^2 \left\{ \epsilon_3(\tau) \frac{1}{\left(1 + \frac{2}{\delta} \frac{R_n}{R_n}\right)} \epsilon_3 \left[\tau \left(1 + \frac{2}{\delta} \frac{R_n}{R_n}\right)^{\frac{1}{2}} \right] \right\} \\ & + \frac{1}{2} \left(\frac{1}{\tau}\right)^2 \left\{ (1 + \tau) e^{-\tau} - \left[1 + \tau \left(1 + \frac{2}{\delta} \frac{R_n}{R_n}\right)^{\frac{1}{2}}\right] \left[e^{-\tau \left(1 + \frac{2}{\delta} \frac{R_n}{R_n}\right)^{\frac{1}{2}}} \right] \right\} \end{aligned} \quad (77)$$

Equation (77) applies to each spectral group with the optical depth τ defined for that group.

For the two high frequency spectral groups, $\tau > 1$ and Eq. (77), for $\delta/R_n \ll 1$ becomes

$$\frac{F}{\pi B} = [1 - 2 \epsilon_3(\tau)] - 2(\delta/R_n) \epsilon_3(\tau) \quad (78)$$

where the first term in brackets in Eq. (78) will be recognized as the tangent slab result. The first frequency group is optically thin, $\tau \ll 1$, for which Eq. (77) becomes

$$\frac{F}{\pi B} = 2\tau g(\delta/R_n) \quad (79)$$

where

$$g(\delta/R_n) = \frac{1}{3(\delta/R_n)} \{ (1 + \delta/R_n)^3 - 1 - [(1 + \delta/R_n)^2 - 1]^{3/2} \} \quad (80)$$

and for $\delta/R_n \ll 1$

$$g(\delta/R_n) = 1 - \frac{2}{3} \sqrt{2} \delta/R_n \quad (81)$$

In Eq. (79), the coefficient 2τ is the result for the tangent slab so that $g(\delta/R_n)$ represents the correction to the tangent slab result due to the concentric sphere geometry. For $\tau > 1$, Eq. (78) shows that the tangent slab is very accurate

for the δ/R_n value of .00346 considered. However, for the optically thin first spectral group, the correction factor is not insignificant even for the small δ/R_n value selected. Applying the optically thin correction to the first spectral group, we determined the exact surface flux from the tangent slab values. Then we performed the three-dimensional numerical calculation using the same constant property, concentric sphere geometry and found:

$$F_{\text{exact}} = 44.8 \text{ kW/cm}^2; F_{\text{numerical}} = 45.4 \text{ kW/cm}^2$$

Hence, the numerical three-dimensional result agrees with the exact value to within roughly 1%. This level of accuracy is certainly adequate for assessing the validity of the one-dimensional transport methods. The numerical (three-dimensional integration) calculation used in the above comparison used $\Delta\phi = 5^\circ$ and a growth rate factor in the θ grid of 1.025. Comparing that result against the standard grid of $\Delta\phi = 10^\circ$ and growth factor 1.05 for the θ mesh, showed only a 1% difference with the coarser grid being closer (fortunately) to the exact result given above. Hence, this somewhat coarser grid was used in the "production" runs discussed below.

4.2 COMPARISON CALCULATIONS

A comparison between the three-dimensional numerical calculation of the net radiative flux and the three one-dimensional approximate models for the shock-body shape of Fig. 2 is shown in Figs. 10, 11 and 12. In each of these comparisons, the one-dimensional fluxes were evaluated at numerous points out to an axial coordinate of $z = 1.0$ and the results are plotted as continuous curves in Figs. 10, 11 and 12. The three-dimensional results were evaluated at six axial points. These are listed below along with the

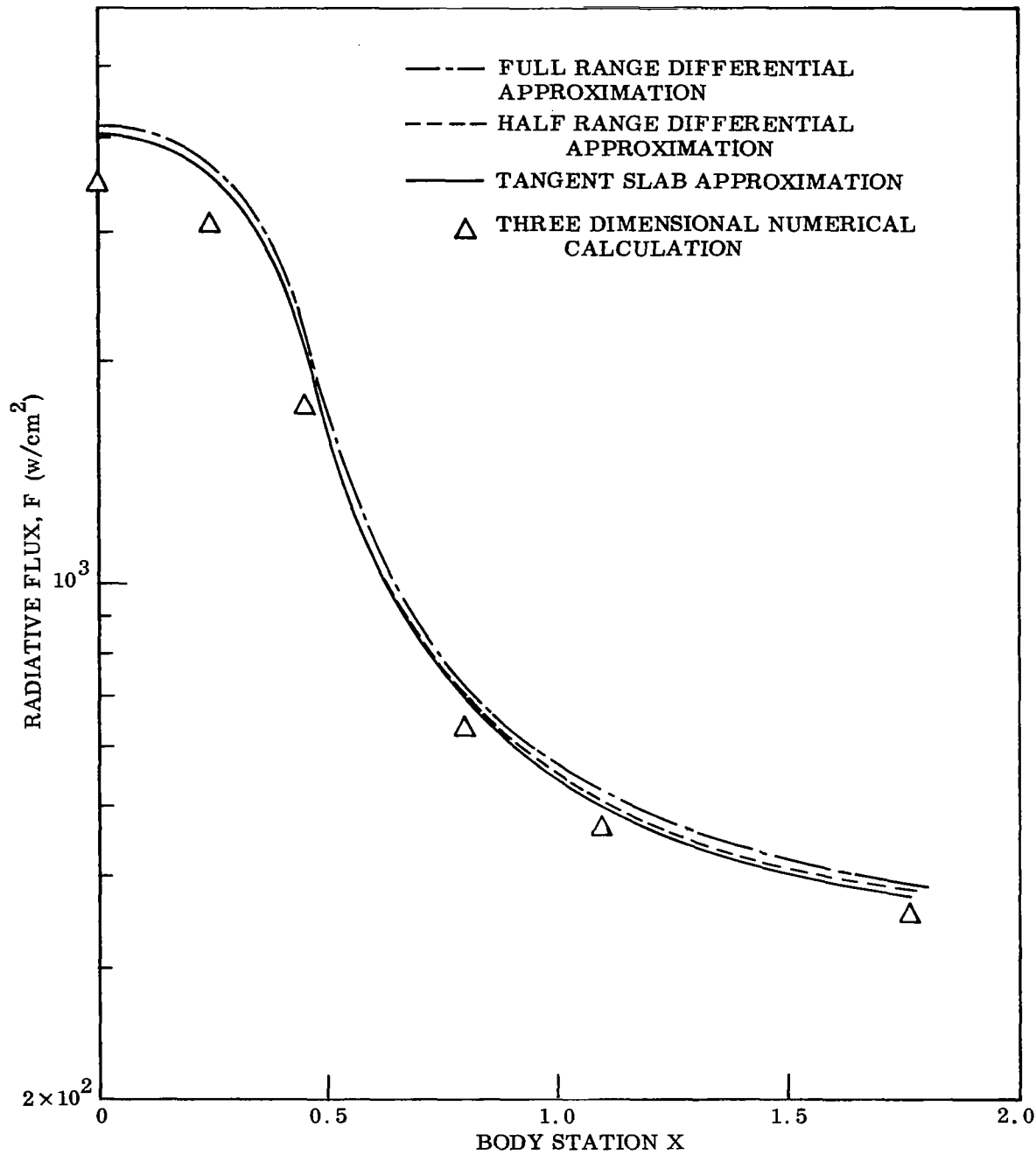


Fig. 10. - Net Surface Flux

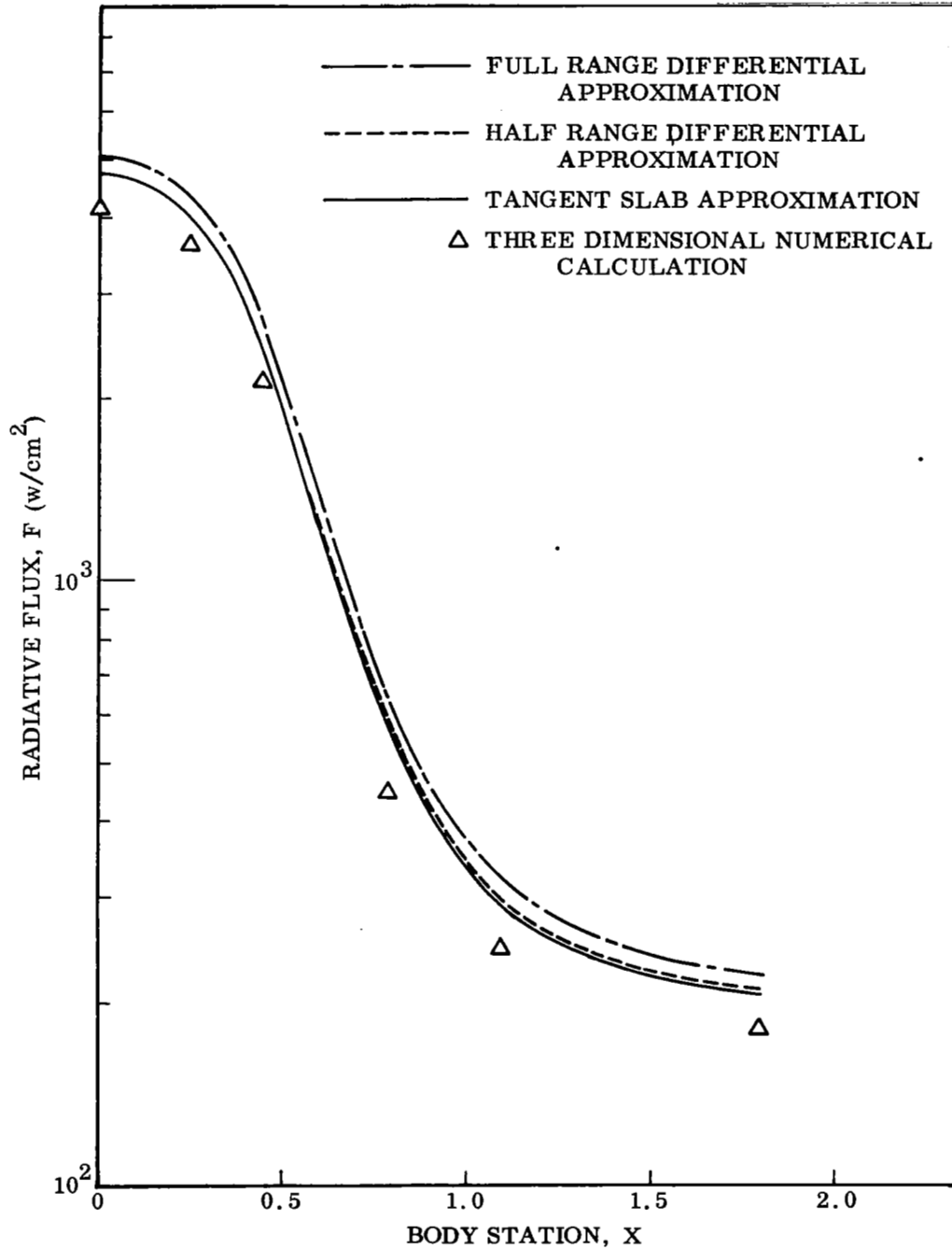


Fig. 11. - Net Midpoint Flux

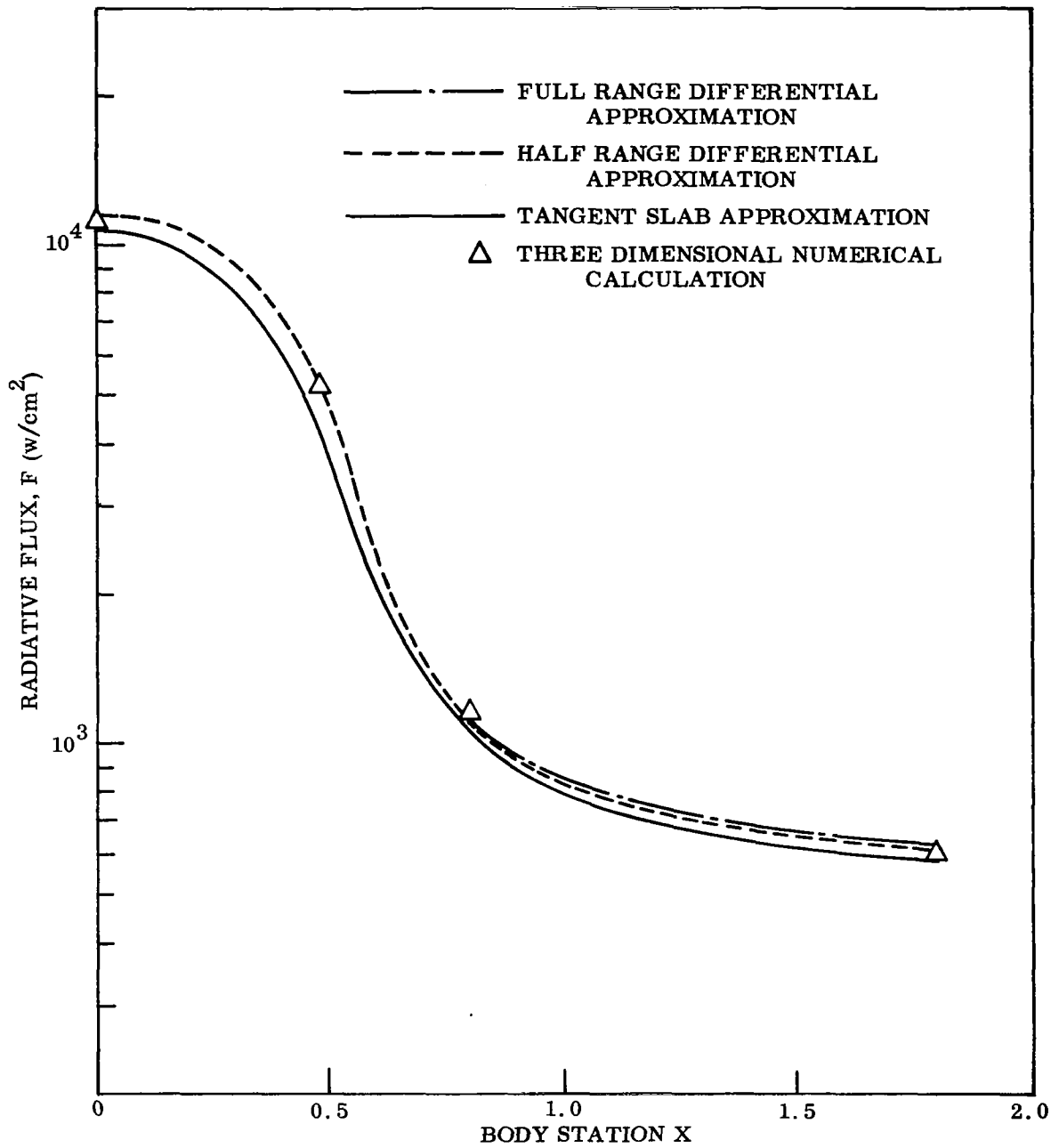


Fig. 12. - Net Shock Flux

corresponding surface coordinate values.

$\frac{z_o = z_b}{}$	$\frac{x}{}$
0	0
.03	.247
.10	.454
.30	.803
.50	1.08
1.00	1.79

Figures 10, 11 and 12 show, respectively, the flux comparison as a function of body location at three shock layer positions: the surface $y = 0$; the shock layer midpoint $y = \delta(x)/2$; and the shock $y = \delta(x)^*$.

Considering first Fig. 10, the surface flux comparison, we note two major facts. One, the error in the various one-dimensional approximations is essentially a maximum at the stagnation point and is nearly constant (on the order of 15%) over the spherical portion of the body. Second, the tangent slab method is consistently the best of the one-dimensional approximations although the half-range differential approximation is quite close to the tangent slab method. The level of error at the stagnation point was an unexpected result. This error is due to the fact that the spectral composition of the flux reaching the surface is dominated by the optically thin first group. For this optically thin condition, the error due to the spherical shell geometry as opposed to the plane parallel geometry implicit in all the one-dimensional methods is roughly given by Eq. (81). For $\delta/R_n = 0.0346$, Eq. (81) yields

*The net flux at the surface and midpoint location is negative, i.e. in the negative y direction.

an estimated error of 17%, the error observed between the three-dimensional and one-dimensional stagnation point calculation. Considering the flux comparison near the tangency point ($z_0 = 0.30$; $x = .80$) we see that the error remains close to that produced by the "geometric effect". Apparently the effect of streamwise temperature variations cancel. Finally, as we proceed onto the conical portion of the body ($z_0 = 1.0$; $x = 1.8$) the geometry becomes more one-dimensional (cf. Fig. 2) and, as expected, the error decreases.

In Fig. 11 we compare the flux at the shock layer midpoint. Near the stagnation point, note that the flux is dominated by the negative component and the error level is close to that for the surface flux. However, on the conical portion of the body, since the enthalpy profile becomes flat (cf. Fig. 9 for $x = 2$), the positive and negative flux components almost cancel. It is not surprising that, for this small flux value, the percentage error will increase. The flux emergent through the shock is shown in Fig. 12. The error in the one-dimensional models is substantially reduced. Clearly this reflects the fact that the emission contributing to the flux originates from the relatively thin, high temperature layer near the shock front. Hence, the emission region is effectively much thinner than the gasdynamical shock layer thickness.

It is the flux divergence term which couples the energy loss or gain into the flow equations. Hence, it is of particular interest to determine how well the one-dimensional models approximate the exact flux divergence result. Such a comparison is shown in Figs. 13, 14 and 15 for the stagnation point ($x = 0$), the tangency point ($x = .80$), and a point on the conical body ($x = 1.8$). The one-dimensional models were evaluated at numerous points across the shock layer at the three selected body locations, and these results provide the

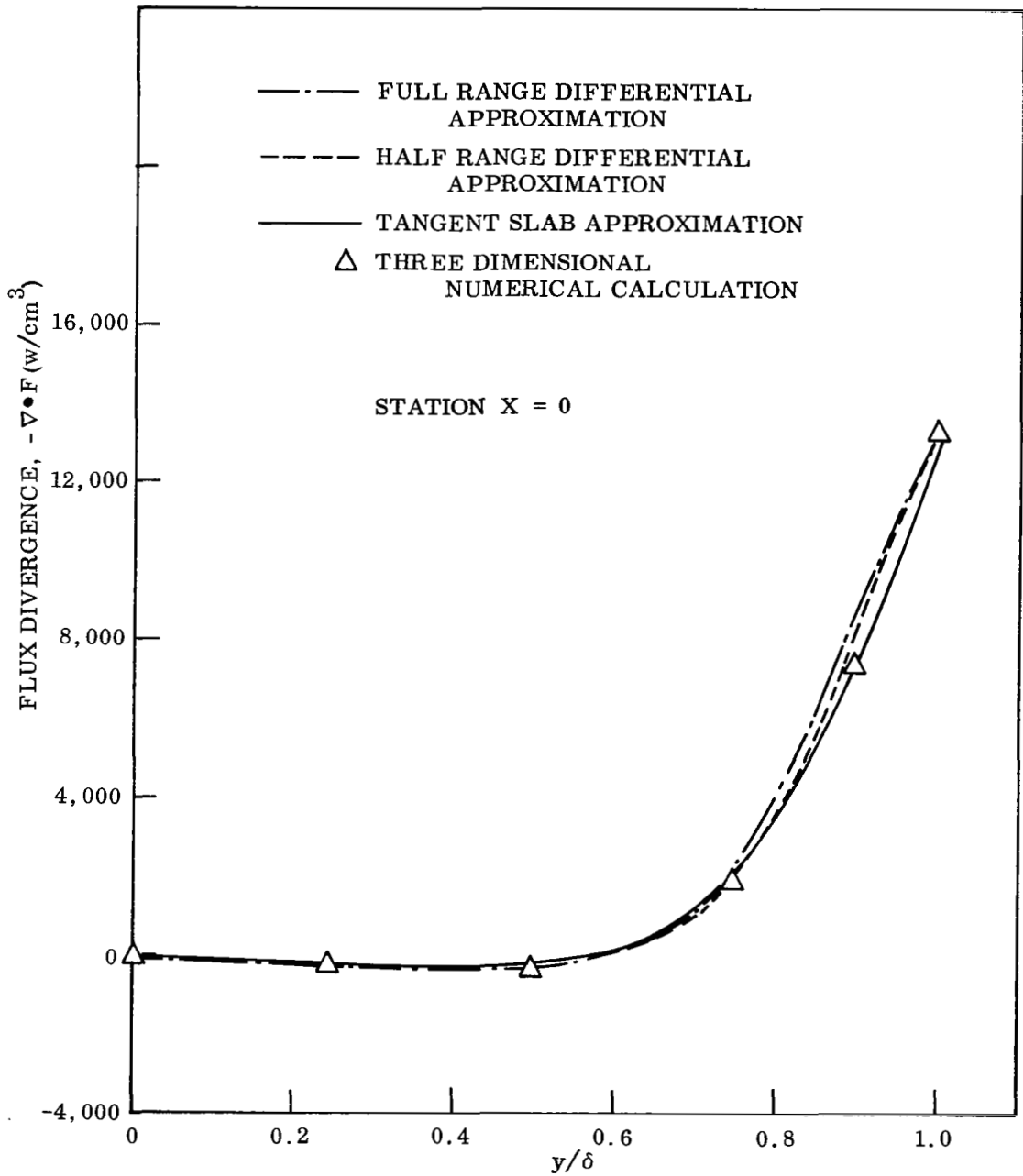


Fig. 13. - Flux Divergence Distribution, X = 0

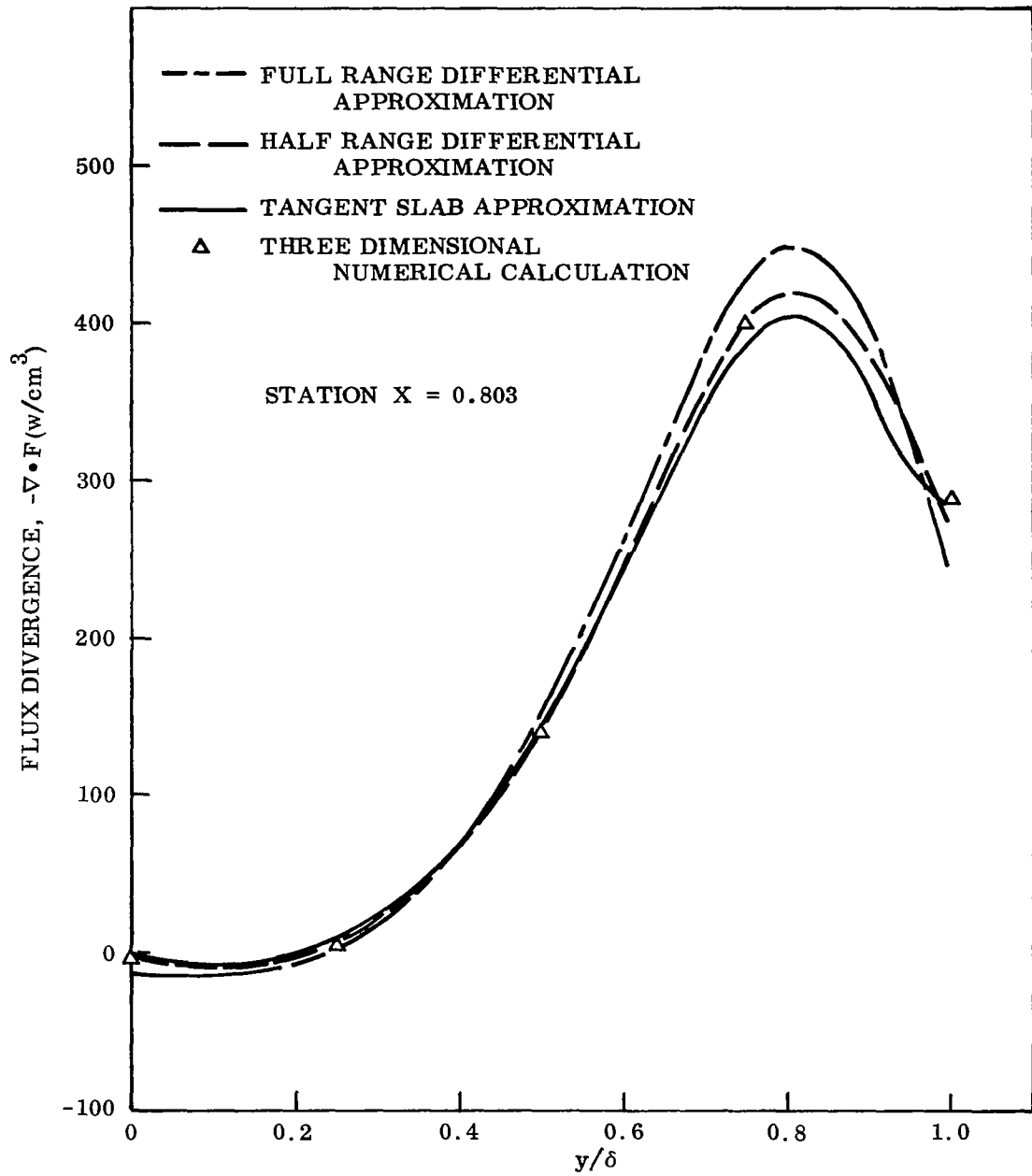


Fig. 14. - Flux Divergence Distribution, X = .803

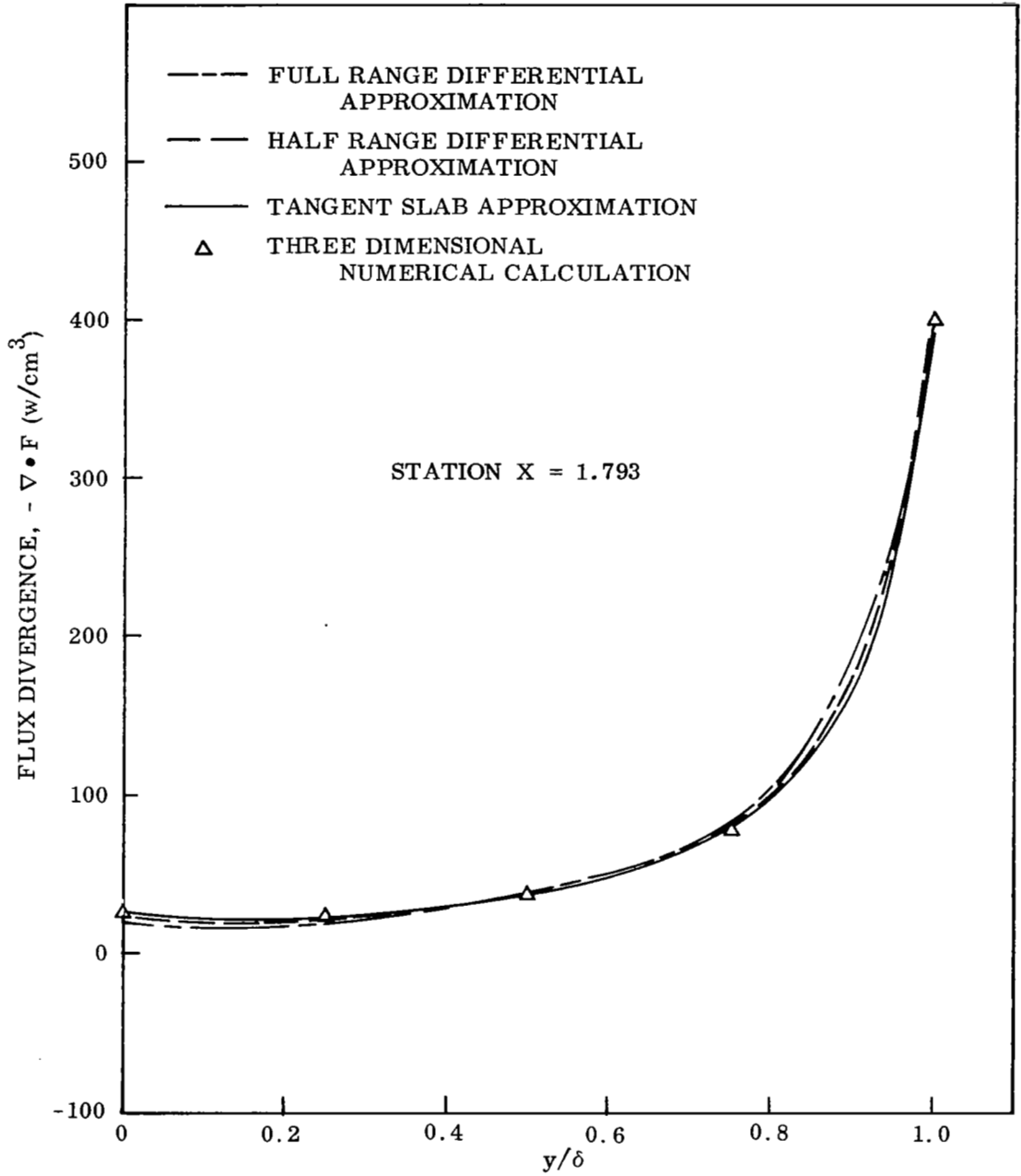


Fig. 15. - Flux Divergence Distribution, X = 1.793

continuous curves shown in Figs. 13, 14 and 15. The three-dimensional calculation was performed at $y/\delta = 0, 0.25, 0.50, 0.75$ and 1.00 at the three selected body locations. Since the flux divergence decays quite rapidly away from the shock at the stagnation point, $x = 0$, an additional three-dimensional calculation was performed at $y/\delta = 0.9$. The one-dimensional models provide a good approximation to the flux divergence throughout the shock layer with the tangent slab method giving consistently the best overall result. The essential reason for the effectiveness of the one-dimensional methods in calculating the flux divergence is that near the shock front, where large energy loss occurs, the flux divergence is dominated by the optically thin term in Eq. (16). Since the total flux emitted from the shock layer can be obtained from a spatial integral of the flux divergence, the accuracy of the one-dimensional methods displayed by Figs. 13,14,15 may appear, at first thought, to be inconsistent with the relative inaccuracy in the surface flux. Recall, however, that the flux out the shock front, which dominates the total energy loss, was accurately predicted by the one-dimensional methods. Moreover, in regions near the surface where the flux divergence is quite small, the relative errors in the flux divergence calculated by the one-dimensional method may be large, although, on an absolute scale, these errors are unimportant.

The fact that the one-dimensional methods are adequate in predicting the radiative energy loss or gain is particularly important. This result allows the one-dimensional methods to be employed in the coupled radiating shock layer flow field calculation with assurance that the resulting thermodynamic structure is accurate. Then, should a more accurate evaluation of the surface flux be desired, one has recourse to performing the detailed three-dimensional calculations

as described in this report.

The results shown to this point have used the shock layer-body geometry shown in Fig. 2. This geometry is certainly a thin layer one ($\delta/R_n = .0346$ at the stagnation point) and hence the question arises as to what increase in error would result for a thicker shock layer configuration. To answer this question, we performed a calculation with the thickness of the shock layer everywhere increased by a factor of two. Hence, at the stagnation point, $\delta/R_n = .0692$, which corresponds quite closely to the normalized shock layer thickness for a Jupiter entry probe where the density ratio across the shock is roughly 10. The thermodynamic properties of the shock layer used in this "thick" layer calculation were calculated from the normalized profiles given in Fig. 9. Hence, in physical coordinates, the temperature profile has been stretched. Results for the surface flux in the thick layer problem are shown in Fig. 16. As expected, the error in the surface flux has increased. At the stagnation point it has increased from 16% for $\delta/R_n = .0346$ to 25% for $\delta/R_n = .0692$. Note, however, that this substantial error for the thick shock layer case is strongly associated with the small optical depth in the spectral region which dominates the surface flux. We performed an additional calculation using $\delta/R_n = .0692$ in which the pressure (and only that parameter) was increased by a factor of 10. The optical depth increased and the error in the tangent slab approximation dropped to 14%.

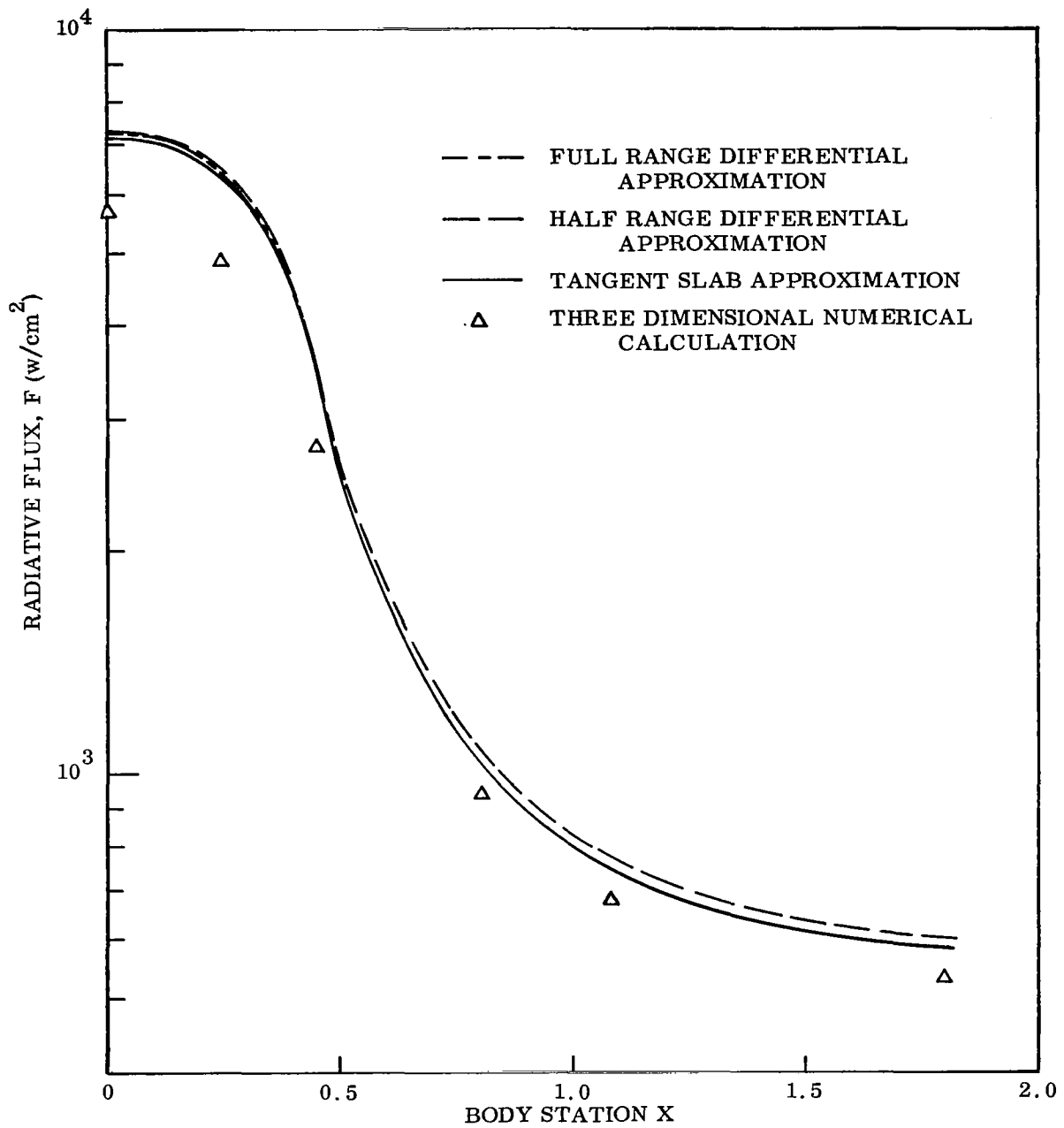


Fig. 16. - Net Surface Flux for the Thick Shock Layer Configuration

5. CONCLUSIONS

Using a shock layer flow field solution and a radiative properties model which capture the essential physical characteristics of high temperature radiating flow, we have quantitatively assessed the validity of one-dimensional methods in evaluating the radiation field. We find that the flux divergence term which couples the radiation field to the energy equation is well approximated by the one-dimensional models, particularly the tangent slab approximation. Then, insofar as determining the flow field properties in a coupled, radiating flow field analysis, the one-dimensional radiative transport model provides accurate results. In calculating the surface radiative flux from a given flow field solution, the one-dimensional models introduce errors on the order of 15% in the hemispherical portion of the body. These errors are a direct consequence of the fact that the surface flux is dominated by the contributions in the optically thin spectral regions. For such optically thin conditions, the errors in the surface flux reflect the deviation of the hemispherical-cap geometry from the plane-parallel geometry.

6. REFERENCES

1. W. A. Page, D. L. Compton, W. J. Borucki, D. L. Ciffone and D. M. Cooper, "Radiation Transport in Inviscid Nonadiabatic Stagnation-Region Shock Layers," AIAA Paper No. 68-784 AIAA 3rd Thermophysics Conference, June 1968.
2. K. H. Wilson, "Massive Blowing Effects on Viscous Radiating Stagnation-Point Flow," AIAA Paper No. 70-203, AIAA 8th Aerospace Sciences Meeting, Jan. 1970.
3. J. H. Chin, "Radiation Transport for Stagnation Point Flows Including the Effects of Lines and Ablation Layer," AIAA J. Vol. 7, pp. 1310, (1969).
4. W. S. Rigdon, R. B. Dirling Jr., and M. Thomas, "Stagnation Point Heat Transfer During Hypervelocity Atmospheric Entry," MDAC Report DAC-63243 and NASA CR-1462, 1970.
5. L. B. Callis, "Time Asymptotic Solutions of Blunt Body Stagnation Region Flows with Nongray Emission and Absorption of Radiation," AIAA Paper No. 68-663, AIAA Fluid and Plasma Dynamics Conference, 1968.

6. L. M. Biberman, S. Ya. Bronin and A. N. Lagor'kov, "Heat Transfer to the Stagnation Point of the Blunt Body in Hypersonic Flow," presented at the 4th International Heat Transfer Conference, Paris, 1970.
7. Y. S. Chou, "On the Thin Shock-Layer Equations for Blunt Body Flow," LMSC Report 6-77-67-24, May 1967.
8. Y. S. Chou and L. H. Blake, "Thin Radiating Shock Layer About a Blunt Body," LMSC Report NASA CR-1547, Mar. 1970.
9. D. H. Sampson, Radiative Contributions to Energy and Momentum Transport in a Gas, Interscience Publ., New York, 1965.
10. W. G. Vincenti and C. H. Kruger, Jr., Introduction to Physical Gasdynamics, John Wiley & Sons, Inc., New York (1965).
11. E. A. Dennon and M. Silbulkin, "An Evaluation of the Differential Approximation for Spherically Symmetric Radiative Transfer," Jo. Heat Trans., Vol. 91, pp. 73-76 (1969).
12. R. F. Clinsnell, "Radiant Heat Transfer in a Spherically Symmetric Medium," LMSC Report 6-76-66-20, Aug. 1966.
13. H. Kennet and S. L. Strack, "Stagnation Point Radiative Transfer," ARS Jo., Vol. 31, pp. 370-372 (1961).

Appendix A
MATHEMATICAL DEVELOPMENTS

In this appendix we summarize the major equations employed in the three-dimensional transport code. The first relations to consider are the angles $\theta^-(\varphi)$ and $\theta^+(\varphi)$ defining the angular region, $\theta^- < \theta < \theta^+$, where rays intersect the body as delineated in the sketch below (this is identical to the view shown in Fig. 4 as discussed in the main text):

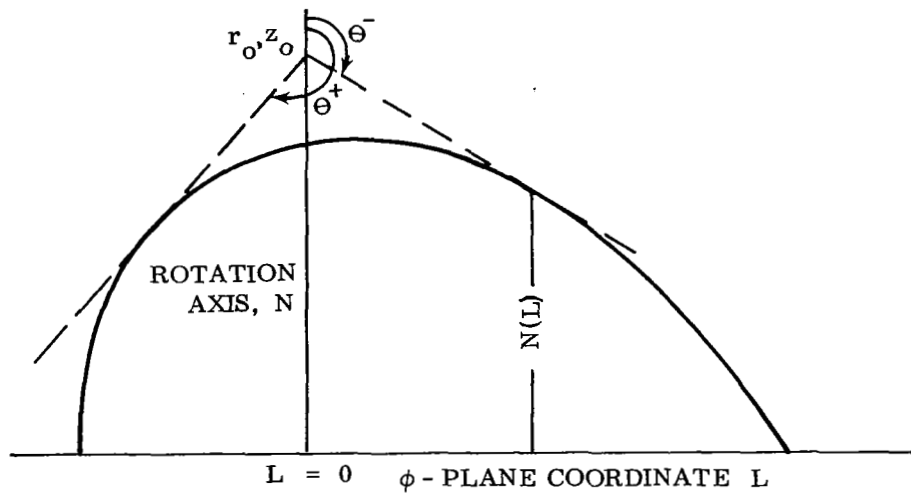


Fig. A-1 - Geometric Interpretation of the Angles θ^- and θ^+

The equation for the body surface $N(L)$ in an arbitrary φ -plane is*

$$N^2 = 2a(z_o + L \sin\varphi) - b(z_o + L \sin\varphi)^2 - L^2 \cos^2\varphi \quad (A-1)$$

* For simplicity we write a and b instead of a_b and b_b since we are only considering the body.

Also geometrically we have at the tangent point

$$\frac{dN}{dL} = \cot \theta \quad (A-2)$$

$$\cot \theta = - \frac{(r_o - N)}{L} \quad (A-3)$$

Combining Eqs. (A-2) and (A-3) to eliminate N , we can obtain a relation between $\cot \theta$ and the distance L at the tangent point. Letting

$$P = \cot \theta \quad (A-4)$$

this relation is

$$L = \frac{(a - bz_o) \sin \varphi - r_o P}{(P^2 + b \sin^2 \varphi + \cos^2 \varphi)} \quad (A-5)$$

We can also combine Eqs. (A-1) and (A-3) to obtain another expression between L and P ,

$$(P^2 + b \sin^2 \varphi + \cos^2 \varphi)L^2 - 2(a \sin \varphi - bz_o \sin \varphi - r_o P)L + (r_o^2 - 2az_o + bz_o^2) = 0 \quad (A-6)$$

We find that Eqs. (A-5) and (A-6) agree, which they must at the tangent point, only when

$$P = \frac{r_o K_o \pm [(r_o^2 - r_b^2)K_o^2 - (r_o^2 - r_b^2)r_b^2 K_1^2]^{\frac{1}{2}}}{r_b^2} \quad (A-7)$$

where $r_b = (2az_o - bz_o^2)^{\frac{1}{2}} \quad (A-8)$

$$K_o = (a - bz_o) \sin \varphi \quad (A-9)$$

$$K_1 = b \sin^2 \varphi + \cos^2 \varphi \quad (A-10)$$

But the above derivation assumed that Eq. (A-1) describes the body contour in the φ -constant plane. However, when the tangent length L is such that the tangent point is on the conical afterbody, i.e., $z_o + L \sin \varphi > z_{t_b}$, then Eq. (A-1) is replaced by

$$N^2 = (L \sin \varphi + r_{t_b} + z_o)^2 - L^2 \cos^2 \varphi \quad (A-11)$$

The derivation proceeds as before and we arrive at an equation identical to Eq. (A-7) except that the coefficients are

$$r_b = r_{t_b} + c_b z_o \quad (A-12)$$

$$K_o = c_b r_b \sin\varphi \quad (A-13)$$

$$K_1 = \cos^2\varphi - c_b \sin^2\varphi \quad (A-14)$$

Finally, identifying P^+ as the value given by Eq. (A-7) using the positive sign and P^- as the value given using the negative sign, we have

$$\theta^- = \cot^{-1}(P^-) \quad (A-15)$$

$$\theta^+ = \pi + \cot^{-1}(P^+) \quad (A-16)$$

The equation defining the limiting value s_m at which the ray intersects the shock or body will be derived next. Referring to Fig. 5 in the main text, note that at any value of s ,

$$r^2(s) = (r_o + s \cos\theta)^2 + (s \sin\theta \cos\varphi)^2 \quad (A-17)$$

But when $s = s_m$ we must also have

$$r^2(s_m) = 2a(z - \delta_o) - b(z - \delta_o)^2 \quad (A-18)$$

where

$$z = z_o + s_m \sin\theta \sin\varphi \quad (A-19)$$

These equations may readily be combined to yield

$$s_m = \frac{-Q_1 \pm [Q_1^2 - Q_2 Q_3]^{\frac{1}{2}}}{Q_3} \quad (A-20)$$

where

$$Q_1 = r_o \cos\theta + \sin\theta \sin\varphi [b(z - \delta_o) - a] \quad (A-21)$$

$$Q_2 = r_o^2 - 2a(z_o - \delta_o) - b(z_o - \delta_o)^2 \quad (A-22)$$

$$Q_3 = \cos^2\theta + \sin^2\theta (b \sin^2\theta + \cos^2\varphi) \quad (A-23)$$

and in Eqs. (A-21)-(A-23) the values for a, b, δ_o appropriate to either the shock or body shape must be applied, depending on the range of the θ variable. Examination of Eq. (A-20) shows that the plus sign is to be used for the shock intersection and the minus sign for the body intersection.

We again note that if the intersection occurs on the conical portion of the shock or body, i.e., $z(s_m) > z_t$, then Eq. (A-20) still holds, but the variables Q_1 , Q_2 and Q_3 become

$$Q_1 = r_o \cos\theta - \sin\theta \sin\varphi c(r_t + cz_o) \quad (\text{A-24})$$

$$Q_2 = r_o^2 - (r_t + cz_o)^2 \quad (\text{A-25})$$

$$Q_3 = \cos^2\theta + \sin^2\theta(\cos^2\varphi - c^2 \sin^2\varphi) \quad (\text{A-26})$$

and in these equations the parameters c and r_t take the values appropriate to the shock or body. Finally, note that from Eq. (A-26) we observe that for $\varphi > \tan^{-1}(1/c)$, Q_3 can become zero and will do so when $\theta = \theta^*$ where

$$\theta^* = \cot^{-1} (c^2 \sin^2\varphi - \cos^2\varphi)^{\frac{1}{2}} \quad (\text{A-27})$$

This expression defines the critical range $\theta^* \leq \theta < \theta^-$ wherein no intersection with the shock or body will occur.

The equations relating the shock layer position (s, θ, φ) to the body-oriented x, y coordinates will be discussed next. The cylindrical r, z coordinates are

$$z(s, \theta, \varphi) = z_o + s \sin\theta \sin\varphi \quad (\text{A-28})$$

$$r(s, \theta, \varphi) = [(r_o + s \cos\theta)^2 + (s \sin\theta \cos\varphi)^2]^{\frac{1}{2}} \quad (\text{A-29})$$

As discussed in the main text (cf. Fig. 6), the key variable is the coordinates of the body point r_b, z_b from which a local normal passes through r, z . From the geometry shown in Fig. 6 we have

$$\tan \delta_b = \frac{z_b - z}{r - r_b} \quad (\text{A-30})$$

But

$$\delta_b = \tan^{-1} \left(\left. \frac{dr}{dz} \right|_{z = z_b} \right)$$

so that

$$\tan \delta_b = \frac{a - bz_b}{r_b} \quad (\text{A-31})$$

where
$$r_b = (2az_b - bz_b^2)^{\frac{1}{2}} \quad (A-32)$$

Equations (A-30)-(A-31) form a set of transcendental relations between δ_b , z_b and r_b which are evaluated as follows. An initial estimate for z_b^i is obtained, the value at the previous point along the ray being the best estimate and the value of z_o being used when the calculation along the ray is initiated. From Eqs. (A-31) and (A-32), δ_b is determined which then allows Eq. (A-30) to be solved for z_b^{i+1} . Of course, this procedure is repeated until convergence is achieved.

The final mathematical point to be discussed is the technique for determining the Δs selection along the ray. Recall that the flow field variation is primarily in the y-direction along the local body normal. Clearly, we wish to select an appropriate Δy increment and determine Δs accordingly. For azimuthal angles $\phi = 90^\circ$ and 0 , the connection between Δs and Δy is quite easy to derive. For arbitrary ϕ , the relation between Δs and Δy is an interesting geometric problem. The key to this problem is to view the projection of the arbitrary θ, ϕ ray on the meridional plane, $\phi = 90^\circ$. This is sketched below.

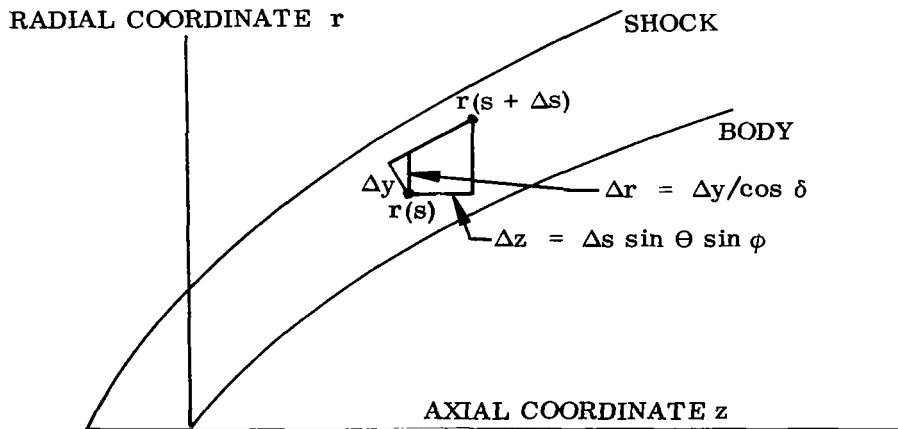


Fig. A-2 - Geometry for Δs Mesh Selection

The change in $r(s)$ can be constructed in two steps. First we have

$$\Delta r_1 = \Delta y / \cos \delta \quad (\text{A-33})$$

which takes us to the point on the meridional plane at fixed z where y has increased the desired Δy increment. Next we move in a direction parallel to the body by an amount

$$\Delta z = \Delta s \sin \theta \sin \varphi \quad (\text{A-34})$$

and, since we are moving parallel, the Δy increment remains fixed. However, as shown in Fig. A-2, the radial coordinate changes by an amount

$$\Delta r_2 = \Delta z \tan \delta \quad (\text{A-35})$$

Hence, we find that

$$r(s+\Delta s) = r(s) + \frac{\Delta y}{\cos \delta} + \Delta s \sin \theta \sin \varphi \tan \delta \quad (\text{A-36})$$

But $r(s+\Delta s)$ can also be related directly to the pathlength position $s+\Delta s$ (cf. Fig. 5 and Eq. (3) of the main text) as

$$[r(s+\Delta s)]^2 = [r_0 + (s+\Delta s) \cos \theta]^2 + [(s+\Delta s) \sin \theta \cos \varphi]^2 \quad (\text{A-37})$$

Equations (A-36) and (A-37) are sufficient to uniquely specify Δs in terms of Δy . We arrive at

$$\Delta s = \frac{-(r_1 - r_2 \cos \theta - s \beta^2) \pm [(r_2 \alpha - r_1 \cos \theta)^2 + \beta^2 (r_1 - s \alpha)^2 - \beta^2 r_0^2]^{\frac{1}{2}}}{(\alpha^2 - \cos^2 \theta - \beta^2)} \quad (\text{A-38})$$

where $r_1 = r(s) + \Delta y / \cos \delta$

$$r_2 = r_0 + s \cos \theta$$

$$\alpha = \sin \theta \sin \varphi \tan \delta$$

$$\beta = \sin \theta \cos \varphi$$

The selection of which sign should be used in front of the radical turns out to depend on whether Δy should be decreasing or increasing, i.e., whether

θ is such that the ray is approaching the body or passing away from the body. Of course, if $\theta^- < \theta < \theta^+$ then the ray is always approaching the body. However, some rays which intersect the shock will first pass close to the body and then go on to the shock. It turns out that just at the point of minimum approach to the body, the radical in Eq. (A-38) passes through zero and at that point the sign in Eq. (A-38) switches from negative to positive. Also, the denominator in Eq. (A-38) can pass through zero when $\phi + \delta \geq 90^\circ$. The value of θ at which the denominator becomes zero corresponds to a condition where θ is such that the ray is parallel to the local body slope. Of course, when the ray is parallel, the Δs value required for a finite Δy change becomes infinite. This problem is easily surmounted by limiting Δs to a maximum Δs_m . Indeed, we have derived the Δs increment solely on the basis of the Δy increment, reflecting the large variation in properties normal to the body. However, streamwise variations also exist and we account for these by always limiting the Δs value from Eq. (A-38) by an a priori bound Δs_m .